JGR Oceans

RESEARCH ARTICLE
10.1029/2023JC019756

Key Points:

- Total air-sea carbon fluxes in the Southern Ocean are altered by up to 66% annually by background mixing variations
- Resolving or skillfully parameterizing the small-scale turbulent mixing in the Southern Ocean is essential to model air-sea carbon fluxes
- Strong vertical gradients in tracer concentrations in the Southern Ocean increase the sensitivity to vertical mixing rates

Supporting Information:

Supporting Information may be found in the online version of this article.

Correspondence to:

E. Ellison,
ece1818@ic.ac.uk

Citation:

Ellison, E., Mashayek, A., & Mazloff, M. (2023). The sensitivity of Southern Ocean air-sea carbon fluxes to background turbulent diapycnal mixing variability. *Journal of Geophysical Research: Oceans*, *128*, e2023JC019756. https://doi.org/10.1029/2023JC019756

Received 27 FEB 2023
Accepted 7 SEP 2023

The Sensitivity of Southern Ocean Air-Sea Carbon Fluxes to Background Turbulent Diapycnal Mixing Variability

Elizabeth Ellison[1], Ali Mashayek[2], and Matthew Mazloff[3]

[1]Department of Civil and Environmental Engineering, Imperial College London, London, UK, [2]Department of Earth Sciences, University of Cambridge, Cambridge, UK, [3]Scripps Institute of Oceanography, University of California San Diego, La Jolla, CA, USA

Abstract The Southern Ocean (SO) connects major ocean basins and hosts large air-sea carbon fluxes due to the resurfacing of deep nutrient and carbon-rich waters. While wind-induced turbulent mixing in the SO mixed layer is significant for air-sea fluxes, the importance of the orders-of-magnitude weaker background mixing below is less well understood. The direct impact of altering background mixing on tracers, as opposed to the response due to a longer-term change in large-scale ocean circulation, is also poorly studied. Topographically induced upward propagating lee waves, wind-induced downward propagating waves generated at the base of the mixed layer, shoaling of southward propagating internal tides, and turbulence under sea ice are among the processes known to induce upper ocean background turbulence but typically are not represented in models. Here, we show that abruptly altering the background mixing in the SO over a range of values typically used in climate models ($\mathcal{O}\left(10^{-4}\right)$ m^2 s^{-1}– $\mathcal{O}\left(10^{-5}\right)$ m^2 s^{-1}) can lead to a ~70% change in annual SO air-sea CO_2 fluxes in the first year of perturbations, and around a ~40% change in annual SO air-sea CO_2 fluxes over the 6-year duration of the experiment, with even greater changes on a seasonal timescale. This is primarily through altering the temperature and the dissolved inorganic carbon and alkalinity distribution in the surface water. Given the high spatiotemporal variability of processes that induce small-scale background mixing, this work demonstrates the importance of their representation in climate models for accurate simulation of global biogeochemical cycles.

Plain Language Summary The Southern Ocean (SO) connects the world's major oceans and plays a crucial role in the exchange of carbon between the atmosphere and the ocean. Vertical mixing in the ocean is responsible for moving both natural dissolved carbon from deeper parts of the ocean to the surface where it can interact with the atmosphere, and anthropogenic carbon from the surface waters into the deep ocean. While we understand the impact of wind-induced mixing in the upper ocean layers on carbon exchange, we know less about the significance of mixing in the ocean interior. By using a model of the SO, we show that adjusting the strength of mixing in the ocean interior causes a significant alteration in the annual exchange of carbon between the ocean and the atmosphere. This study highlights the importance of accurately representing the strength of ocean interior mixing in climate models to improve our understanding of carbon exchange between the atmosphere and the ocean.

1. Introduction

The Southern Ocean (SO), defined here as any region south of 30°S, is a key region for the global carbon cycle due to the upwelling of deep, old, carbon, and nutrient-enriched waters, connecting the vast reservoir of nutrients and carbon from below the mixed layer with the surface (Talley et al., 2016). The deep ocean interacts with the atmosphere through less than 4% of the ocean's surface area (Klocker, 2018; Watson & Naveira Garabato, 2006), with 65% of interior waters making first contact with the atmosphere in the SO (DeVries & Primeau, 2011). As the deep ocean contains up to 60 times more carbon than the atmosphere (Arias et al., 2021), small perturbations to air-sea carbon fluxes can be important for atmospheric carbon content (Adkins, 2013). Therefore, the SO, and especially the upwelling branch of circumpolar deep water (Marshall & Speer, 2012), is key in controlling global biogeochemical cycles, the exchange of CO_2 between the atmosphere and the deep ocean, atmospheric CO_2 levels, and the response of the ocean and atmosphere to climate change (Gruber et al., 2019; Sarmiento et al., 2004).

Several expeditions have revealed strong cross-density (diapycnal) mixing due to small-scale ocean turbulence in the SO (Garabato et al., 2004, 2019; Ledwell et al., 2011; Watson et al., 2013), though measurements remain sparse and difficult to scale up (Cael & Mashayek, 2021; Mashayek et al., 2017, 2022; Tamsitt et al., 2018). Given the small scales of diapycnal mixing, it is not resolved in operational models, and so it is parameterized (Gaspar et al., 1990; Large et al., 1994) in two forms.

1. Surface mixed layer mixing from storms and other surface winds, as well as convective instabilities.
2. Background turbulence induced by bottom-generated internal waves due to interaction of jets, eddies, and tides with rough topography or due to shoaling and breaking of remotely generated internal tides (see Baker & Mashayek, 2021, 2022; de Lavergne et al., 2020 for reviews of such dynamics).

The "background" mixing in the ocean interior is typically several orders of magnitude smaller than that in the surface mixed layers. Since the seminal work of Munk (1966), bulk measurements of ocean mixing have found a diapycnal turbulent diffusivity of $K_v \sim \mathcal{O}(10^{-4})\ \mathrm{m}^2\ \mathrm{s}^{-1}$ required to resurface the abyssal waters and facilitate the closure of the meridional overturning circulation (MOC) (Ganachaud & Wunsch, 2000; Lumpkin & Speer, 2007; Talley, 2013; Talley et al., 2003), while estimates from profiling instruments often find $K_v \sim \mathcal{O}(10^{-5})\ \mathrm{m}^2\ \mathrm{s}^{-1}$ in the interior of the ocean and much larger values of $K_v \sim \mathcal{O}(10^{-3})\ \mathrm{m}^2\ \mathrm{s}^{-1}$ only in the 200 m directly above the seafloor (Waterhouse et al., 2014). In the Diapycnal and Isopycnal Mixing Experiment in the SO (DIMES), estimates of mixing from microstructure profiles measurements in the interior of the Drake Passage reported $K_v \sim \mathcal{O}(10^{-5})\ \mathrm{m}^2\ \mathrm{s}^{-1}$. Meanwhile, the dispersion of an anthropogenic tracer, released where these measurements were made, suggested the tracer itself experienced a higher mixing rate of $K_v \sim \mathcal{O}(10^{-4})\ \mathrm{m}^2\ \mathrm{s}^{-1}$ at the average depth of tracer at ~2 km (Mashayek et al., 2017; Watson et al., 2013). The background values used in models typically lie within this range.

Though diapycnal mixing is highly temporally and spatially variable due to its generating mechanisms (e.g., strong surface westerly winds and the interaction of currents and eddies with rough topography), it is frequently parameterized as temporally invariable and, at times, even spatially constant. Current best estimates of SO diapycnal mixing are based on "static" maps, produced with numerous limiting assumptions, approximating the contributions from topographically generated lee waves (Nikurashin & Ferrari, 2011; Shakespeare, 2020), wind-induced near-inertial waves (Alford, 2020), and internal tides (de Lavergne et al., 2020). These maps have formed the basis of our representation of such processes in earth system models (Melet et al., 2014, 2022). The choice of initial background mixing rates in ocean models is a large source of uncertainty, and model solutions using background mixing values ranging from 10^{-5} to $10^{-4}\ \mathrm{m}^2\ \mathrm{s}^{-1}$ are all physically plausible.

Diapycnal mixing in the global ocean interior is known to be an important factor in variations in atmospheric carbon levels on centennial to millennial timescales via alterations in ocean circulation (Marinov & Gnanadesikan, 2011; Sigman et al., 2010). Enhanced diapycnal mixing increases deep ocean ventilation via the SO and reduces ocean carbon storage through biological and solubility carbon pumps (Marinov et al., 2008; Marinov & Gnanadesikan, 2011). Climate models are sensitive to the intensity and distribution of global diapycnal mixing, accounting for about 25% of the uncertainty in the estimated range of atmospheric CO_2 concentrations by 2100 (Schmittner et al., 2009). In this work, we are concerned with the immediate response of the air-sea carbon fluxes to altered mixing below the surface mixed layer on timescales much shorter than those explored in the above-mentioned works. It is the immediate response of the system to altered background mixing that is our focus, not a longer-term equilibrated state. We also solely focus on mixing in the SO which has been assumed to be of secondary importance for the global ocean circulation (Nikurashin & Ferrari, 2013) but significant for setting global tracer distributions (Ellison, Cimoli, & Mashayek, 2023).

Given the strong wind-driven isopycnal upwelling in the SO, and the intense diapycnal mixing within the mixed layer induced by strong winds, one may imagine that the shift in the background mixing rate below the mixed layer from 10^{-4} to $10^{-5}\ \mathrm{m}^2\ \mathrm{s}^{-1}$ would be inconsequential for setting the air-sea fluxes of CO_2 on short timescales. In this work, we show the contrary.

The air-sea flux of CO_2 primarily depends on the difference in the partial pressures of CO_2 (pCO_2) between the atmosphere and the ocean. Physical and biological processes, including advective and diffusive transport of tracers, organic matter formations and sinking, and the dilution of tracers due to precipitation, runoff and sea ice melt, all alter the pCO_2 of surface waters (Mahadevan et al., 2011), resulting in high variability in time and space of the CO_2 fluxes in the SO (Rosso et al., 2017). The influence of altering background diapycnal mixing on the surface ocean $p\mathrm{CO}_2$ is complex to predict due to spatiotemporal variability in biological and physical responses to variations in mixing (Dutreuil et al., 2009), and the coupled multivariate dependency of ocean $p\mathrm{CO}_2$ to temperature, salinity, alkalinity, and dissolved inorganic carbon.

In this work, we will show that an abrupt perturbation of the background mixing strongly alters the SO-integrated air-sea CO_2 fluxes on seasonal, annual, and interannual timescales.

2. Experiment Setup

We use the Biogeochemical SO state estimate (B-SOSE; Verdy & Mazloff, 2017). The interaction between diapycnal mixing below the mixed layer, the mixed layer dynamics, and the mesoscale processes that advect tracers prove essential for the problem under consideration here.

The state estimate is produced by solving for the model initial and boundary conditions, the so-called model “controls,” which minimize a weighted least squares sum of model-observation misfits. This is achieved using an adjoint model that provides the gradients of the misfit function with respect to the model controls, allowing those controls to be efficiently and systematically determined. The model is run for 7 years (2012–2018) using the adjoint method-based assimilation product. This includes physical and biogeochemical constraints obtained from Argo floats, including biogeochemical parameters from the SOCCOM float array, satellite altimetry, satellite SST, and ship transect data. The full set of model parameters used in this 1/6° setup is given in Swierczek et al. (2021); see Verdy and Mazloff (2017) for initial conditions.

The resulting product is a closed-budget model simulation of SO biogeochemistry, including air-sea fluxes of heat and carbon and the cycling of nutrients from a biogeochemical and carbon model. Because it represents the constantly evolving present SO, it is not in a steady state, in contrast to what one may expect from analysis of an earth system model undergoing a long spin-up process.

The model domain extends from the equator to 78°S with 52 vertical layers of varying thickness. The zonal grid spacing is always 1/6°, but the meridional grid spacing changes with the cosine of the latitude. Ocean physics is represented using the MITgcm. The ocean is forced through an atmospheric boundary layer scheme where bulk formulae determine heat fluxes, freshwater (salt), and momentum (Large & Yeager, 2009). The hourly atmospheric conditions of ERA5 (Dee et al., 2011) are applied, with adjustments added that were determined by optimization (Verdy & Mazloff, 2017) using the adjoint method. Sea ice is modeled using 0-layer thermodynamics (Fenty & Heimbach, 2013) and an implicit Line Successive Over Relaxation (LSOR) dynamical solver (Losch et al., 2010). A horizontal biharmonic diffusivity is used with a value of $10^{-8}\ \mathrm{m}^4\ \mathrm{s}^{-1}$. Implicit vertical diffusivity for convection is set to $10\ \mathrm{m}^2\ \mathrm{s}^{-1}$, and no mesoscale eddy parameterization was implemented. For further details, see Verdy and Mazloff (2017) and Swierczek et al. (2021).

The parameterization of diapycnal mixing is composed of two parts. The GGL90 mixed layer parameterization of Gaspar et al. (1990) is used to represent parameterized turbulence and is highly surface-enhanced (Figure 1d), inducing strong turbulence under the seasonal atmospheric storm tracks, mixing the DIC gradients in the upper few hundreds of meters. In other places, such as under the ice or when there is no strong wind-induced turbulence, the models rely on a prescribed background value for turbulent diffusivity. The background value is behind the sensitivity of fluxes discussed in this work. As discussed in subsequent paragraphs, the background vertical diffusivity is altered in each experimental run. The background mixing value is added to the GGL90 mixing to achieve a total vertical diapycnal mixing value.

The Biogeochemistry with LIght, Nutrients and Gases (NBLING) model, described fully in Verdy and Mazloff (2017), forms the biochemical framework within B-SOSE. The original BLING model described in Galbraith et al. (2010) was modified (for B-SOSE) with the addition of nitrogen cycling and improvements in the representation of phytoplankton population dynamics and particle export (Bianchi et al., 2013; Galbraith et al., 2015). Biological activity influences the concentrations of carbon and oxygen. At the core of the BLING model is primary production with limitations by light, nitrate, phosphate, iron, and temperature, and subsequent remineralization of organic matter back to inorganic nutrients. Nine prognostic tracers are simulated in NBLING: dissolved inorganic carbon (DIC), alkalinity (ALK), oxygen (O_2), nitrate (NO_3), phosphate (PO_4), iron (Fe), dissolved organic nitrogen (DON), dissolved organic phosphate (DOP), and phytoplankton biomass. The biomass partitioning into species is determined using stored ratios updated every time step based on growth and decay

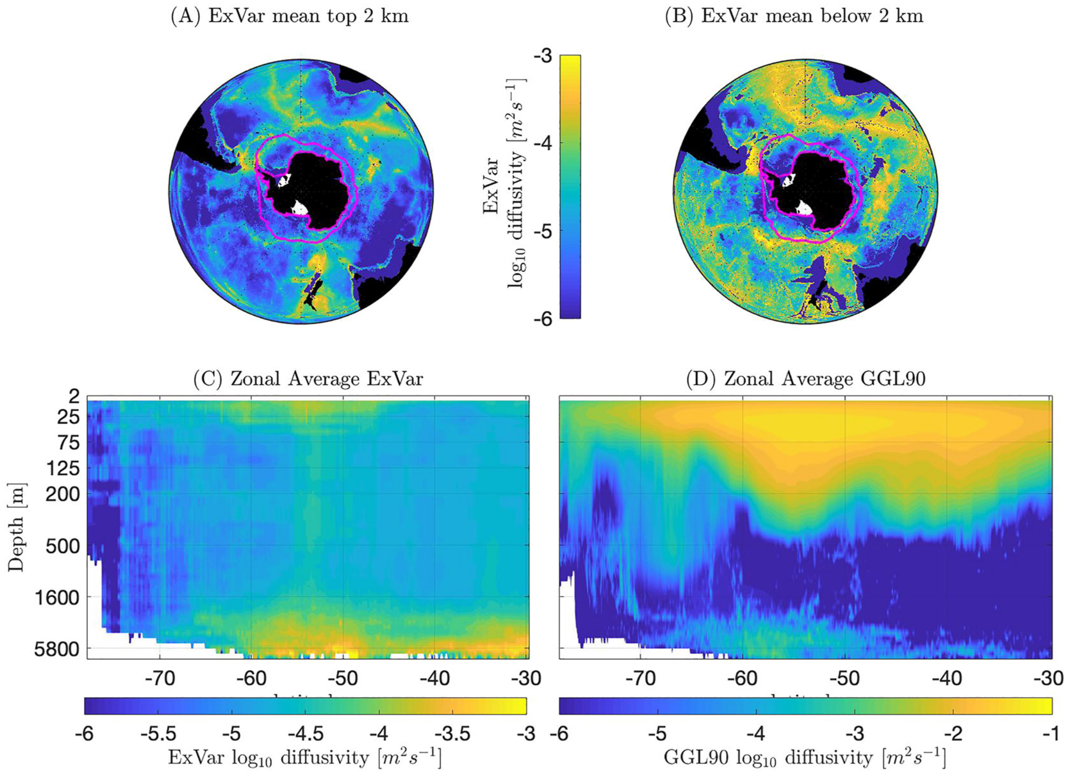

Figure 1. Diapycnal mixing in the Southern Ocean State Estimate (SOSE). The distribution of diapycnal mixing in the Southern Ocean, constructed as the sum of contributions from tides and topographically generated lee waves. This mixing is shown averaged in depth over the top/bottom 2 km in panel *A*/*B*, and zonally over the Southern Ocean in (c). These maps are used in the spatially variable mixing map experiment (ExVar). For reference, a zonally averaged map of the storm-induced mixing, as parameterized through GGL90 parameterization in B-SOSE, is also shown in panel (d). The pink lines on (a) and (b) show the annual mean extent of sea ice. Note that the range of the color bar in panel (d) is different from the other panels.

rates. We include three types of phytoplankton: large, small, and diazotrophs. Small cells represent calcifying organisms; they use calcium carbonate to form shells. Diazotrophs can fix nitrogen, so nitrate availability does not limit them. Phytoplankton loss is expressed as a power law with a size-dependent exponent based on Dunne et al. (2005).

The B-SOSE carbon system is adapted from the MITgcm simple biogeochemical model of Dutkiewicz et al. (2006). DIC and ALK are prognostic variables, and pH and $p\mathrm{CO}_2$ are diagnosed based on Follows et al. (2006), making oceanic $p\mathrm{CO}_2$ a function of DIC, ALK, temperature (T), salinity (S), and silica, where silica is prescribed from the 2013 World Ocean Atlas climatology (Garcia et al., 2013). CO_2 and O_2 air-sea fluxes are calculated following Wanninkhof (1992). Atmospheric $p\mathrm{CO}_2$ is prescribed using values from the CarbonTracker product (Peters et al., 2007).

The B-SOSE's original conditions and atmospheric adjustments were obtained using 10^{-4} m^2 s^{-1} as the value for background diapycnal diffusivity (added to the GGL90 mixing). The initial condition comes from a tuned 2008–2013 run, and small and smooth adjustments are made to this state in the adjoint method optimization. The adjustments do result in some transient waves, but these have a negligible impact on the monthly average diagnostics we analyze in this work. We refer to that base simulation as Ex1e-4 hereafter. We have chosen a background mixing value of 10^{-4} m^2 s^{-1} for this initial base simulation, as B-SOSE has been used and validated extensively against both physical and biogeochemical observations using this value as the background mixing rate (Mazloff et al., 2010; Verdy & Mazloff, 2017). Therefore, using 10^{-4} m^2 s^{-1} as our spin-up background mixing rates allows our results to be as comparable with this available literature as possible.

This base simulation is not in equilibrium, as it assimilates a wide range of temporally variable data. Using the same initial conditions and atmospheric state adjustments, two additional model simulations were carried out for

2013–2018. In these subsequent runs, the system experiences a step-function kick due to the altered background mixing, representative of the constantly changing background mixing rate of the ocean. In this paper, we examine the immediate response of tracers to the change in this background mixing rate.

The first perturbation experiment, Ex1e-5, uses a constant background diffusivity value of 10^{-5} m^2 s^{-1}. The range 10^{-5} to 10^{-4} m^2 s^{-1} is sandwiched between the two canonical paradigms of mixing often considered in Physical Oceanography. The third experiment, ExVar, uses a spatially variable (but temporally constant) vertical diapycnal mixing map (Figures 1a–1c). The ExVar map is constructed as the sum of contributions from tides (de Lavergne et al., 2020) and topographically-generated lee waves (Nikurashin & Ferrari, 2011) and features horizontal and vertical variations over a range much broader than 10^{-5} to 10^{-4} m^2 s^{-1}. The tidally generated mixing estimate is composed of the contributions of local (high-mode) and long-distance propagating (low-mode) internal tides, taking into account wave-wave interactions, scattering by abyssal hills, dissipation over critical slopes, shoaling, and the propagation of the wave. Compared with the dissipation measured by microstructure profilers and parameterized mixing rates from Argo float data, there is good agreement (de Lavergne et al., 2020). The lee wave generated estimate is based on the energy conversion from tidal and geostrophic motions into internal waves combined with a turbulent mixing parameterization. This is achieved using estimates of the energy conversion into internal waves by tides and geostrophic motions combined with a parameterization to estimate the rate of mixing generated by these waves (Nikurashin & Ferrari, 2011).

In ExVar, the mean diapycnal mixing rate the upper 2 km is generally less than 10^{-4} m^2 s^{-1}, and is lower than 10^{-5} m^2 s^{-1} in large regions. The ExVar diapycnal mixing rate is as high as 10^{-3} m^2 s^{-1}, higher than Ex1e-4, but only in small areas (Figure 1a). Therefore, in most areas, the background mixing rate in ExVar is more similar to Ex1e-5 than Ex1e-4. Although background mixing values dominate over the GGL90 parameterization in middepths, GGL90 is orders of magnitude larger than the background mixing value in the upper ocean (Figure 1d). The three cases together allow an evaluation of the response of carbon fluxes in the model to a temporal variation in background mixing.

3. Results

3.1. Carbon Fluxes

The SO is a net sink of atmospheric CO_2, with most of the uptake occurring between 50°S and 30°S, with a peak at 40°S, where around 0.007 Pg C/yr is taken up (Figure 2a). 40°S is the average latitude of the subtropical front, separating the subtropical waters from the subantarctic mode waters, thus hosting rich mesoscale and submesoscale frontal dynamics and enhanced air-sea exchange of tracers. To the south of the polar front (PF), on the other hand, the upwelling of deep carbon-rich waters causes carbon outgassing (Figure 2e, shown in red). Additional uptake occurs further south around Antarctica due to downwelling (induced by a change in the wind direction from westerly to easterly) and deepwater formation. Thus, SO fronts, which mark sharp gradients in temperature and carbon chemistry, separate regions of net uptake from regions of outgassing. Higher latitudes show very low mean annual carbon fluxes, partly due to seasonal ice cover.

Carbon uptake varies year-on-year during the 6 years of the state estimate run by almost 0.002 Pg C/yr at some latitudes, with especially high interannual variability at 60°S and 40°S (Figure 2a). The interannual range of carbon fluxes for Ex1e-5 is nonmonotonic, as the sign of the changes from year to year varies.

Alterations to background diapycnal mixing alter SO carbon fluxes, with ExVar showing smaller differences from Ex1e-4 than Ex1e-5 (Figure 2b dashed versus solid lines). The sensitivity to altered diapycnal mixing is variable throughout the 6 years (Figure 2b). This interannual range in sensitivity of around 1×10^{-5} Pg C/yr is well within the interannual variability of zonally integrated carbon fluxes in Ex1e-5, which has a mean standard deviation of 2.5×10^{-4} Pg C/yr over all latitudes for 2013 to 2018 (Figures 2a and 2b). A higher difference between Ex1e-5 and Ex1e-4, and between ExVar and Ex1e-4 occurs in the first 3 years (2013–2015) than in the last 3 years (2016–2018) (Figure 2b). As upper ocean mixing is never in an equilibrium state due to constantly changing winds, eddies and buoyancy fluxes, the response to the mixing perturbation over the first 3 years of this experiment do not seem unrealistically exaggerated.

Decreasing the background mixing from Ex1e-4 to Ex1e-5 leads to an increase in annual mean zonally integrated carbon uptake at all latitudes (Figures 2c and 2f). The most significant reduction is around 55°S (Figures 2c

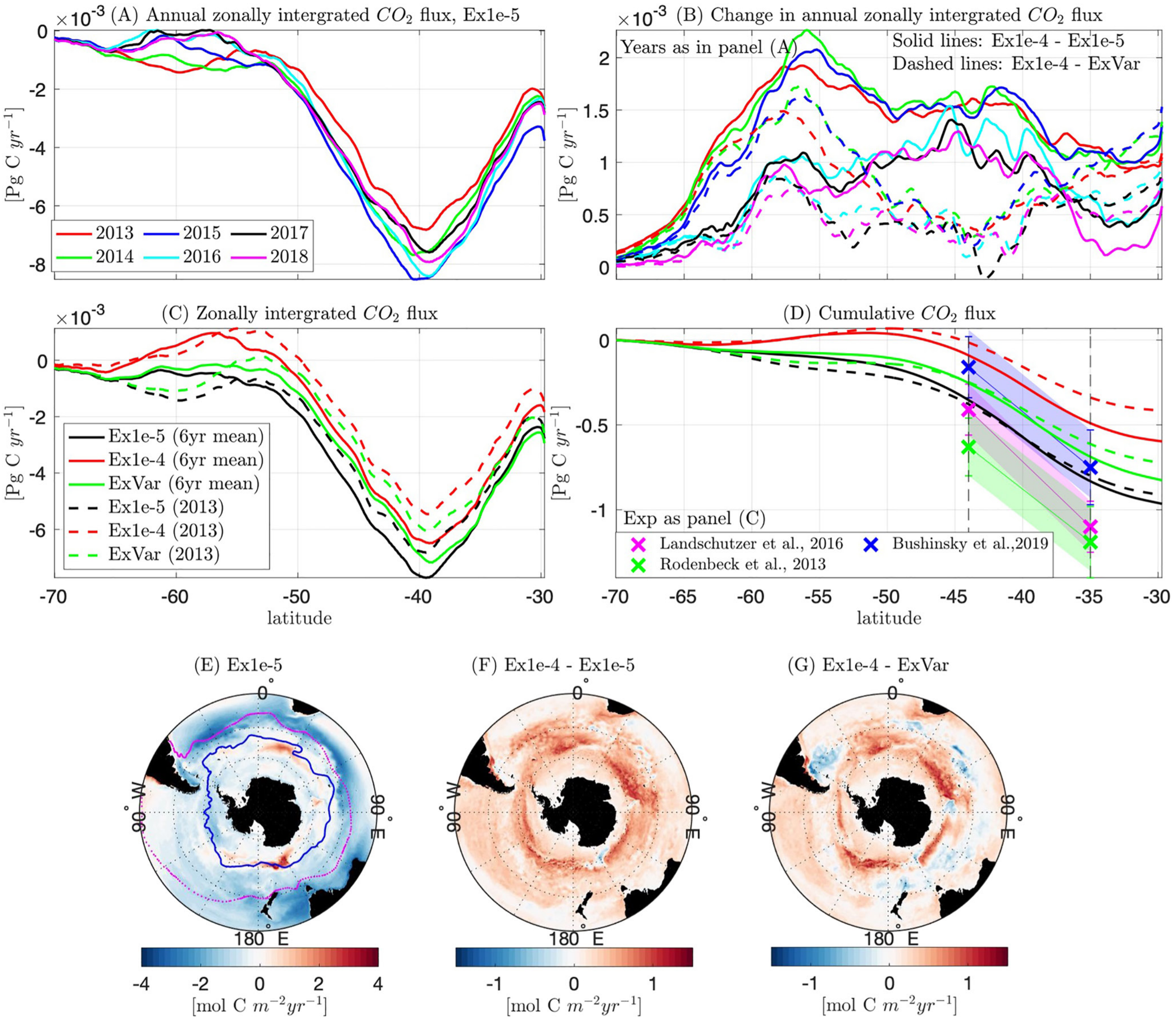

Figure 2. (a) Zonally integrated flux of Carbon for each year of Ex1e-5 (negative = Carbon flux from atmosphere to ocean). (b) The difference in the zonally integrated flux of Carbon between Ex1e-4 and Ex1e-5 (solid lines) and Ex1e-4 and ExVar (dashed lines) for each year of the experiment. (c) Zonally integrated annual mean Carbon flux for Ex1e-4, Ex1e-5, and ExVar over the 6-year period (2013–2018) and for the first year of the experiment (2013). (d) Annual mean (averaged over 2013–2018) cumulative integral of carbon fluxes from 70°S northward to 30°S (legend same as the previous panel). Observational markers are included for comparison (Bushinsky et al., 2019; Landschützer et al., 2016; Rödenbeck et al., 2013). The Landschützer et al. (2016) estimate utilized the Surface Ocean CO_2 Atlas (SOCAT) Version 2 database (Bakker et al., 2016), while the Rödenbeck et al. (2013) estimate used SOCAT Version 1.5 database. The Bushinsky et al. (2019) estimate utilized data from floats deployed by the Southern Ocean Carbon and Climate Observations and Modeling (SOCCOM) project (Johnson et al., 2017) as well as the SOCAT database. (e) Average annual carbon flux for Ex1e-5, the blue line shows the Polar Front, the magenta line shows Subtropical Front as defined by Orsi et al. (1995). (f) Annual mean change in Carbon flux (Ex1e-4–Ex1e-5). (g) Annual mean change in Carbon flux (Ex1e-4–ExVar). Positive values imply reduced carbon uptake or increased outgassing.

and 2f). Minor changes occur south of 65°S due to the ice cover. In ExVar, the most significant changes from Ex1e-4 occur around the PF. North of 50°S, the difference between ExVar and Ex1e-4 is far smaller (Figures 2c and 2g).

In Ex1e-5, the mean annual cumulative net flux of carbon into the ocean, integrated from 75°S northward to 30°S, is 1 Pg C/yr (Figure 2d). In Ex1e-4 only 0.6 Pg C/yr is taken up, a reduction of 0.4 Pg C/yr. The annual uptake of ExVar falls between the other two experiments at around 0.8 Pg C/yr. These numbers are for the 6-year mean, and as panel B shows, the reductions from Ex1e-5 are much higher over the first 3 years (almost double).

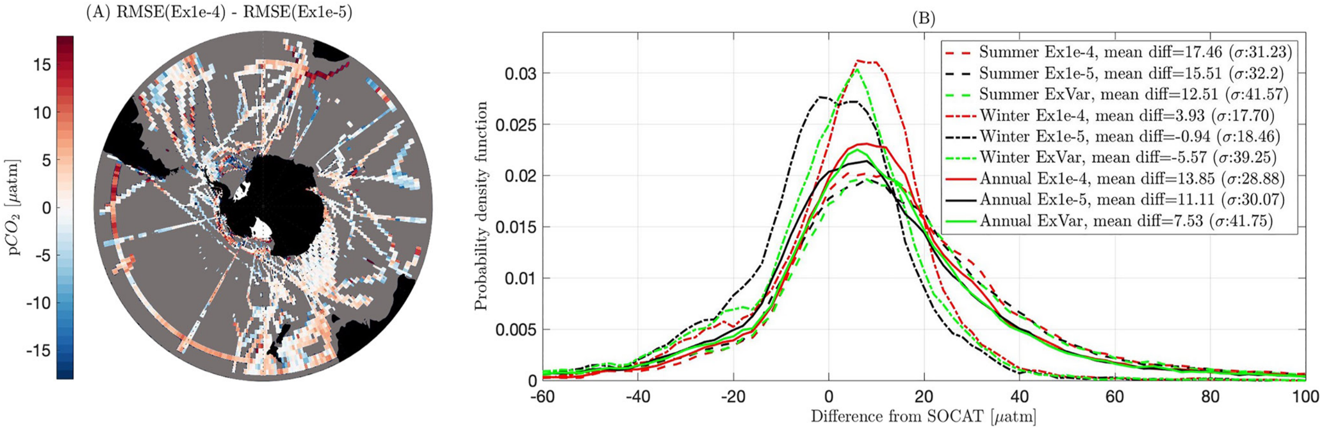

Figure 3. Comparison of modeled $p\mathrm{CO}_2$ to observations from Surface Ocean CO_2 Atlas (SOCAT) between 2012 and 2018 (Bakker et al., 2016). (a) Comparison of the root mean squared error between Ex1e-4 and Ex1e-5. Red/blue shows regions where Ex1e-5/Ex1e-4 is closer to the observations. (b) Probability density function showing the misfit between observed $p\mathrm{CO}_2$ from SOCAT and the model outputs for $p\mathrm{CO}_2$ in Ex1e-5 (black), Ex1e-4 (red), and ExVar (green).

The cumulative carbon fluxes are compared to other estimates of the integrated SO carbon flux from 75°S northward to up to 45°S and 35°S for the period 2015–2017 (Figure 2d; Bushinsky et al., 2019; Landschützer et al., 2016; Rödenbeck et al., 2013). At 45°S, the Ex1e-5 cumulative flux lies between the three observationally inferred estimates, while the ExVar flux is slightly lower, with Ex1e-4 being the lowest of all three, well below the estimates of the other studies. At 35°S, there is a larger range in carbon uptake between the three model runs. Ex1e-5 is the only experiment that lies within the bounds of the three observational estimates, while the lower carbon uptake of ExVar and Ex1e-4 are outside the range of previous estimates. The difference between the cumulative carbon fluxes at 45°S of the three experiments is similar to the uncertainty associated with prior estimates. All experiments fall within the uncertain range of the Bushinsky et al. estimate at 35°S, but ExVar and Ex1e-5 are also within the Landschützer et al. estimate. At 45°S ExVar and Ex1e-5 are within the uncertainty range of the Bushinsky et al. estimate but are lower than the other estimates available for this period. This comparison to previous estimates suggests that Ex1e-4 underestimates the annual mean SO carbon uptake.

3.2. Comparison to $p\mathrm{CO}_2$ Observational Data

The $p\mathrm{CO}_2$ values for Ex1e-4, Ex1e-5, and ExVar can be compared to 2013–2018 observed levels from the Surface Ocean CO_2 Atlas (SOCAT) (Bakker et al., 2016) (Figure 3). Neither matches SOCAT observations better than the other (Figure 3a). Regional trends are also unclear, although, from the limited data available, Ex1e-5 appears to represent better the $p\mathrm{CO}_2$ of the northern Pacific Ocean and off the coast of South Africa and Tasmania. Meanwhile, estimates from Ex1e-4 are better matched to observations in the western Atlantic and the northern Indian Oceans.

The probability density function for the difference between SOCAT and B-SOSE for the three experiments is broken down over seasons (Figure 3b). In summer, the standard deviation of differences between ExVar and data is much larger than those for Ex1e-4 and Ex1e-5. The mean difference of 15.5 µatm for Ex1e-5 is lower than 17.46 µatm for Ex1e-4, while ExVar has the lowest mean difference from observations. The high-end tails of the distributions are more skewed than the lower ends, implying a systematic overestimate of $p\mathrm{CO}_2$ by B-SOSE. B-SOSE overestimates the flux of carbon from the ocean to the atmosphere or underestimates the SO carbon uptake from the atmosphere, particularly in the summer.

SOCAT data are heavily biased toward summer data due to limitations on data collection in the winter. The mean difference between SOCAT and B-SOSE is lower for the winter mean than for the summer in all experiments. In the winter, ExVar has the largest mean difference from observations but also the largest standard deviation. In an annual mean sense, ExVar does a better job in matching SOCAT observations, though with a much higher standard deviation. It is interesting to note that, while in the annual mean sense, ExVar better matches SOCAT observations of $p\mathrm{CO}_2$, Ex1e-5 was better able to replicate previous observational estimates of cumulative SO CO_2 fluxes (Figure 2d).

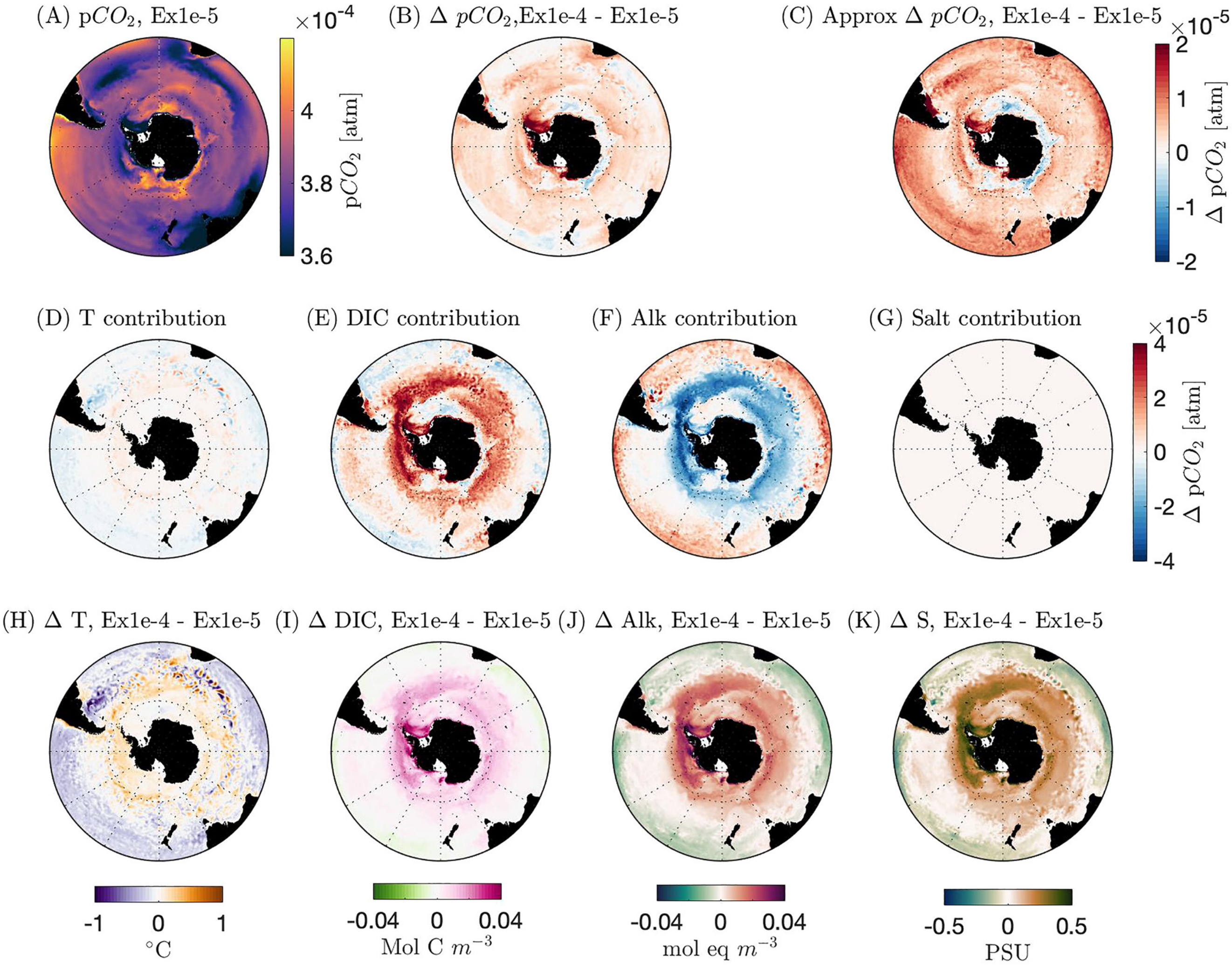

Figure 4. Changes to surface ocean partial pressure. (a) Annual mean surface ocean pCO$_2$ in Ex1e-5. (b) Change in pCO$_2$ between Ex1e-4 and Ex1e-5. (c) Same as panel b, but this time changes to pCO$_2$ approximated based on the methodology of Takahashi et al. (2014) that breaks down the change into various contributions as per Equations 1–5. The various contributions are shown in panels (d–g). (h–k) Changes in annual mean DIC, alkalinity, potential temperature, and salinity.

3.3. Changes to Surface Ocean pCO$_2$

Given that ExVar estimates of carbon fluxes fall between those of Ex1e-4 and Ex1e-5, hereafter, we only focus on the differences between Ex1e-4 and Ex1e-5. Air-sea carbon fluxes exist due to the difference in pCO$_2$ between the atmosphere and the surface ocean. The high (low) surface ocean pCO$_2$ values result in regions of low (high) oceanic uptake or even outgassing of CO$_2$ from the atmosphere (Figure 4a). A region of exception is under sea ice, where the diffusive flux of gases is prevented. The changes in carbon fluxes due to altered mixing, as in Figure 2, are due to changes in surface ocean pCO$_2$, as atmospheric conditions are constant across experiments.

The annual mean pCO$_2$ of the surface ocean is higher in Ex1e-4 than in Ex1e-5 in almost all regions, reducing the pCO$_2$ gradient and carbon uptake (Figure 4b). The areas of greatest increase in pCO$_2$ include south of South Africa and the waters east of the West Antarctic Peninsula. Small regions where the annual mean pCO$_2$ is reduced in Ex1e-4 include latitudes of around 30°S, especially to the east of Australia, the Argentine basin, and a few small bands just off the coast of Antarctica in the south.

Using the methodology set out by Takahashi et al. (2014), we break down the pCO$_2$ change to contributions from changes in the upper ocean content of salinity, temperature, DIC and alkalinity (Equation 1). The change in pCO$_2$ as a contribution from each of the four tracers is calculated using Equations 2–5, where $\bar{p}$CO$_2$ is the mean pCO$_2$,

$\bar{A}lk$ is the mean alkalinity, γ_{CO_2} is the Revelle factor for CO_2 (value used = 11), and γ_{ALK} is the Revelle factor for alkalinity (value used = −10):

$$\Delta p\mathrm{CO}_2 = \left(\frac{\delta p\mathrm{CO}_2}{\delta T}\right)\Delta T + \left(\frac{\delta p\mathrm{CO}_2}{\delta DIC}\right)\Delta DIC + \left(\frac{\delta p\mathrm{CO}_2}{\delta Alk}\right)\Delta Alk + \left(\frac{\delta p\mathrm{CO}_2}{\delta S}\right)\Delta S \tag{1}$$

$$\frac{\delta p\mathrm{CO}_2}{\delta T}\Delta T = 2(p\mathrm{CO}_2)[Exp(0.0423(\pm 0.0002)\Delta T/2) - 1] \tag{2}$$

$$\left(\frac{\delta p\mathrm{CO}_2}{\delta DIC}\right) = \gamma_{\mathrm{CO}_2}\left(\bar{p}\mathrm{CO}_2/\bar{T}\mathrm{CO}_2\right) \tag{3}$$

$$\frac{\delta p\mathrm{CO}_2}{\delta Alk} = \gamma_{ALK}\left(\frac{\bar{p}\mathrm{CO}_2}{\bar{A}lk}\right) \tag{4}$$

$$\left(\frac{\delta p\mathrm{CO}_2}{\delta S}\right) = 0.026(\pm 0.002)\cdot \bar{p}\mathrm{CO}_2 \tag{5}$$

The four individual contributions, shown in Figures 4d–4g, can be summed together to give the annual mean approximated change in pCO_2 (Figure 4c). This calculated change agrees satisfactorily with the changes in pCO_2 between the two experiments (Figure 4b), although the calculated changes are generally larger than the observed changes. This verifies the assumptions made in Equations 2–5, and confirms that changes to the distribution of these tracers are key in causing changes to carbon fluxes (Figures 4b and 4c). The only region where the Takahashi et al. method does not capture the changes is in the north of the SO, west of New Zealand and east of South America in the Argentine basin. This is likely due to enhanced water mass mixing occurring in these regions, making changes in this area complex to approximate with simple assumptions. While the calculations shown in Figure 4 use the upper 2.6 m of the water column, they are not sensitive to depth and similar results are found down to ∼55 m.

On an annual basis, contributions from changes in DIC and alkalinity concentrations are the main drivers of changes in pCO_2 (Figures 4e and 4f), with the contributions from salinity and temperature being secondary (Figures 4d and 4g). An increase in the alkalinity content decreases pCO_2, while an increase in salinity or DIC increases pCO_2. Where the temperature increases, pCO_2 increases due to modulation of the equilibrium DIC. The increase in the DIC content of the surface waters of the southern SO in Ex1e-4 increases pCO_2, while in the north the decrease in DIC concentration decreases pCO_2. On the contrary, the increase in alkalinity concentration in the south decreases pCO_2, while the decrease in alkalinity in the north increases pCO_2. Changes in salinity concentrations act to slightly increase the pCO_2 in Ex1e-4. Temperature changes with enhanced mixing cause a slight decrease in pCO_2 in the north and an increase in pCO_2 in the south in Ex1e-4.

The initial changes in the upper ocean temperature, salinity, DIC, and alkalinity are due to alterations to the diapycnal flux of these tracers. The diapycnal flux for a tracer with concentration C may be approximated by $-K_v \times \frac{\partial C}{\partial z}$. Therefore, if vertical diapycnal mixing (K_v) is increased, more tracer, for example, DIC, is mixed downgradient (upward into the surface waters). This increase in upward flux is the strongest where the vertical gradients are the strongest. Therefore, strong correlations develop between locations with sharp vertical gradients and locations with significantly altered tracer content with altered background mixing (Figures 5a–5d). This correlation is especially clear when examining changes to tracer distributions in the first month of the perturbation experiments, as shown in Figure 5. Changes over the full 6-year period are shown in Figure S2 in Supporting Information S1). Over time, the carbonate chemistry of the surface waters is altered by indirect changes, such as the horizontal advection of tracers, causing the correlation between vertical gradients and changes in tracer concentrations to become less pronounced.

Regions that experience high changes in DIC concentration with enhanced mixing are around the coast of Antarctica, south of 60°S and above depths of 40 m. In these areas, surface waters are fed by wind-induced upwelling of deep waters rich in DIC due to the respiration of organic material. Further to the north, the upper 120 m of the water column has weak vertical gradients of DIC concentration (Figures 5e and 5f). The dipole pattern shown when looking in a zonal average sense implies the erosion of the sharp gradient by enhanced mixing, allowing the vertical tracer gradients to be stronger in the lower mixing scenarios of Ex1e-5 and ExVar. The DIC

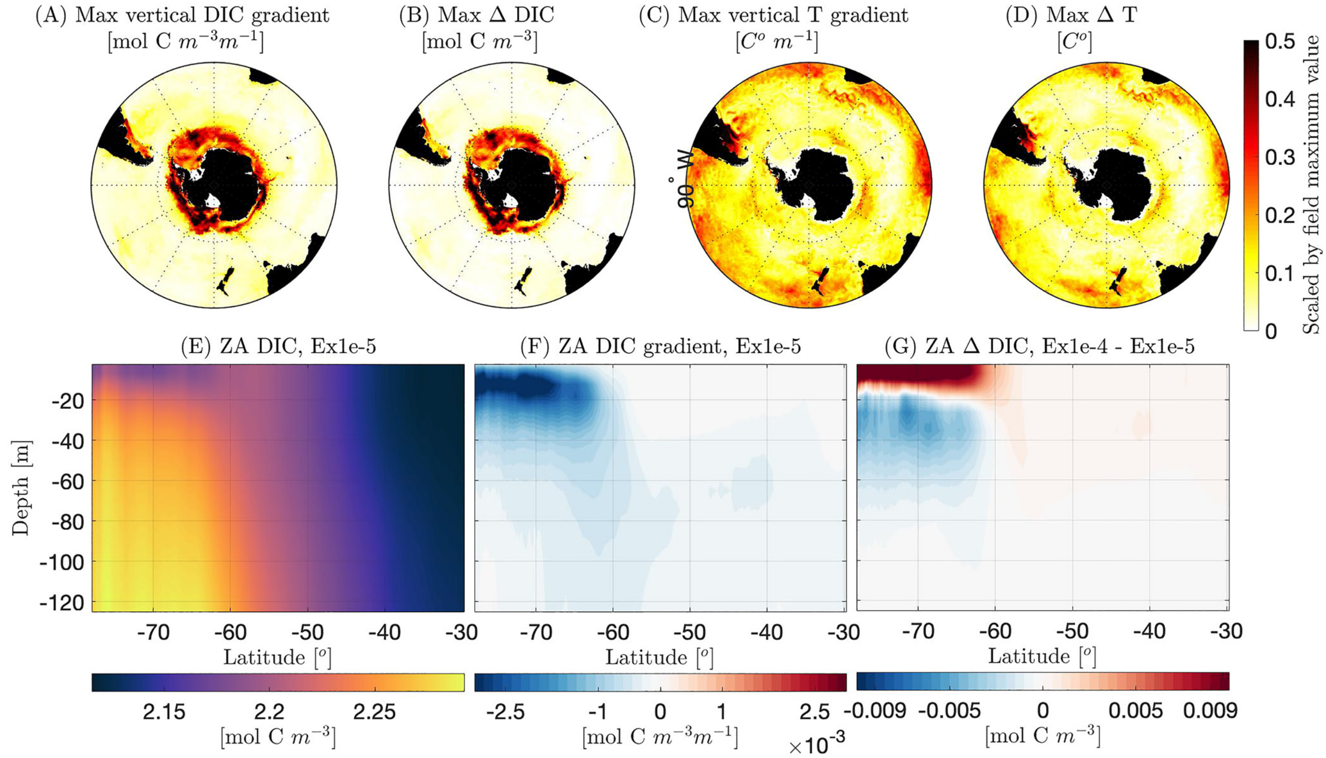

Figure 5. (a) Maximum vertical dissolved inorganic carbon (DIC) gradient in the water column for Ex1e-5, scaled by the maximum DIC vertical gradient of the field. (b) Maximum change in DIC between Ex1e-4 and Ex1e-5, scaled by the maximum difference in DIC of the field. (c, d) Same as (a and b) but for temperature. The maximum change in DIC (temperature) is defined as the greatest difference in DIC (temperature) concentration between the two experiments at any depth above 200 m at each latitude and longitude in the domain. All values are scaled by the maximum value of the field, with the colorbar ranging from 0 to 0.5. (e) Zonal average (ZA) DIC concentration in Ex1e-5. (f) Zonal average DIC vertical gradient in Ex1e-5; blue indicates a decrease in concentration toward the surface. (g) Zonally averaged change in DIC concentration (Ex1e-4–Ex1e-5). All are shown for December 2012, the first month of all experiments.

concentration increases with increased mixing in the upper surface waters (shown in red), while concentrations decrease between 40 and 20m depth (shown in blue) due to a flux divergence, as more of this carbon has been mixed upwards into the surface waters (Figure 5g). There is a clear divide at around 20 m; this depth corresponds to the depth of the maximum vertical gradient. Changes in alkalinity and salinity roughly follow a pattern similar to DIC (shown in Figure S1 in Supporting Information S1). The greatest changes in temperature occur in different regions, mainly in the northern SO, especially at around 90°E, in the Argentine basin, and in the waters surrounding New Zealand.

3.4. Temporal and Seasonal Variability of Changes in $p\mathrm{CO}_2$

Carbon fluxes show strong seasonal and spatial variations (Figure 6), as discussed in Rosso et al. (2017). In the austral summer (December to February), the SO from 60°S to 30°S is a net source of CO_2 outgassing (Figures 6a and 6b, dashed lines). Some outgassing also occurs at the upwelling zone of the PF, especially in the Atlantic basin (Figure 6c). South of ~60°S, the SO acts as a slight carbon sink even in summer. Austral winter (June to August) has much higher carbon uptake than summer, with the net uptake occurring in almost all regions of the SO, except beneath sea ice (Figures 6a, 6b, and 6d). Small outgassing regions exist around the polar front and at the upwelling region off the west coast of South America in the Argentine basin (Figure 6d).

While Figures 2 and 4 show the changes to carbon fluxes between model runs in an annual mean sense, there are also significant temporal patterns in how mixing perturbation alters carbon fluxes (as will be shown in Figure 9). Figures 6 and 7 examine the dominant mechanisms for seasonal differences observed in the changes to $p\mathrm{CO}_2$ between Ex1e-4, ExVar, and Ex1e-5. The changes in carbon fluxes between experiments are greater in winter than in summer (Figures 6a, 6e, and 6f). An exception is in the very south, where ice cover during winter reduces gas exchange in all experiments. In winter, Ex1e-4 has a reduced carbon uptake compared to Ex1e-5, while ExVar

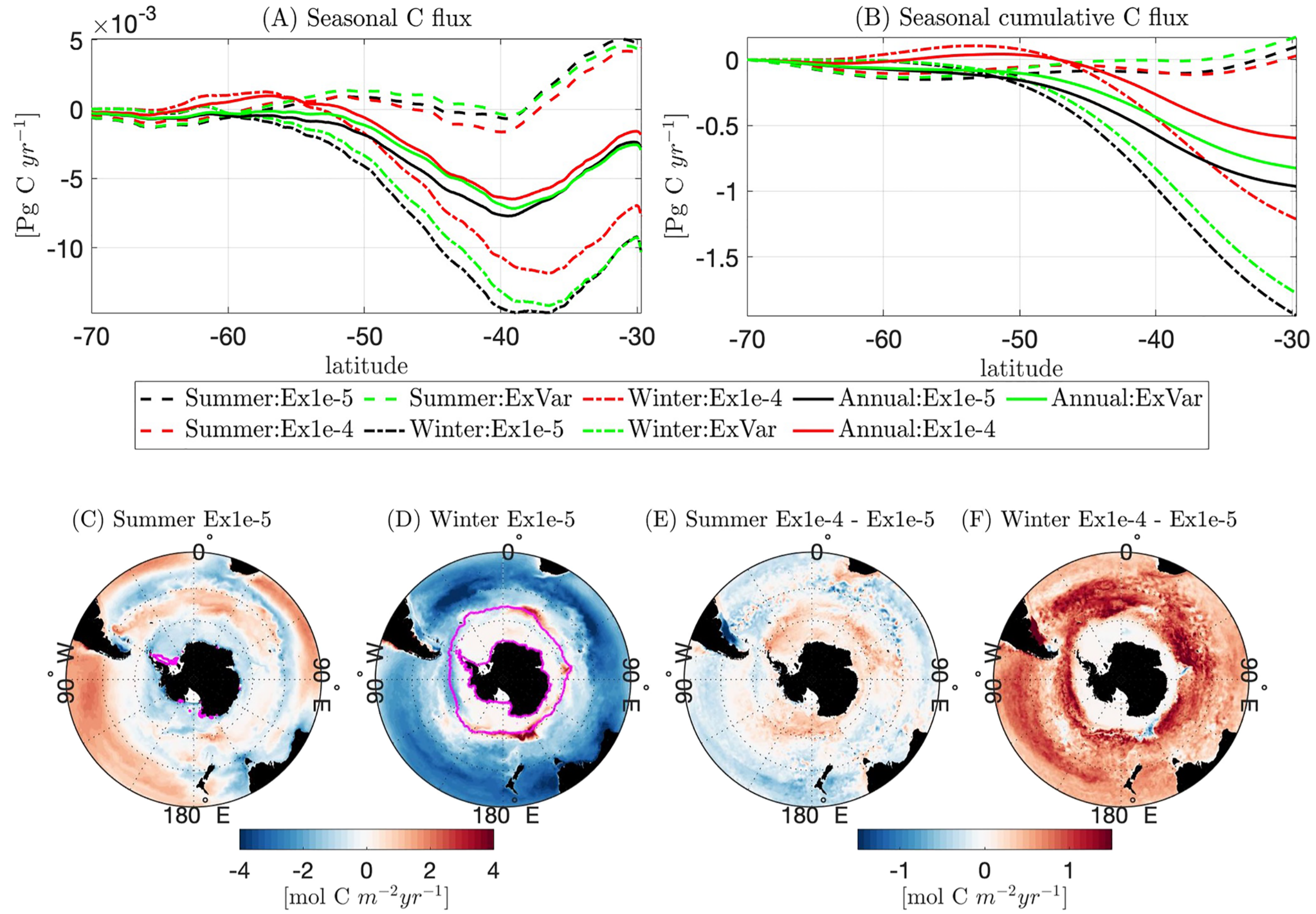

Figure 6. (a) Zonally integrated Carbon flux for Ex1e-4, Ex1e-5, and ExVar for summer (dashed), winter (Dotted), and annual mean (solid line). (b) The cumulative sum of carbon fluxes from 70°S northward to 30°S (legend same as the previous panel). (c) Average summer carbon flux for Ex1e-5; magenta lines show the minimum summer ice extent. (d) Average winter carbon flux for Ex1e-5; magenta lines show the maximum winter ice extent. (e) Mean change in summer Carbon flux (Ex1e-4–Ex1e-5). (f) Mean change in winter Carbon flux (Ex1e-4–Ex1e-5). Positive values imply reduced carbon uptake or increased outgassing.

has a similar carbon uptake to Ex1e-5 (Figure 6a). Cumulatively integrated winter carbon fluxes are reduced from almost 2 Pg C/yr in Ex1e-5 to 1.2 Pg C/yr in Ex1e-4. The greatest decreases in uptake occur around 40°S. The Argentine basin is also a region of pronounced diminished carbon uptake (Figure 6f). Three small areas on the edge of the winter ice extent experience increased carbon uptake in the winter due to reduced ice cover, which will be discussed later in this section (Blue areas, Figure 6f). Summer changes to carbon fluxes are of a smaller magnitude and show more spatial variability than the winter months (Figures 6a and 6e). In summer, the cumulative intergrated outgassing of Ex1e-5 is higher than Ex1e-4, and ExVar is higher than both Ex1e-4 and Ex1e-5, though the difference between all three runs is less than 0.2 Pg C/yr. At lower latitudes where the SO is a net source of carbon to the atmosphere, outgassing is decreased in Ex1e-4. Further south, where the SO is a carbon sink, CO_2 uptake is reduced in Ex1e-4 (Figure 6e). Changes in flux occur as far south as the Antarctic continent due to diminished summer sea ice.

Using Equations 1–5 and Figure 4, we next use the Takahashi et al. methodology to examine seasonal changes to tracer contributions and their implications for the $p\mathrm{CO}_2$ and carbon fluxes. The outcome is shown in Figure 7. Salinity contributions to changes to $p\mathrm{CO}_2$ are not shown as they are negligible compared to DIC, alkalinity, and temperature contributions. The temperature contribution varies greatly between seasons, being stronger in January than in July (Figures 7b and 7e). Closer to Antarctica, changes in temperature increase the $p\mathrm{CO}_2$ of Ex1e-4 surface waters in both seasons. In July, this positive contribution extends further north. In January, the change in temperature causes very strong reductions in $p\mathrm{CO}_2$, especially in the subtropical gyres. Because the change in surface temperature and associated change to $p\mathrm{CO}_2$ vary with season, the annual mean change in temperature

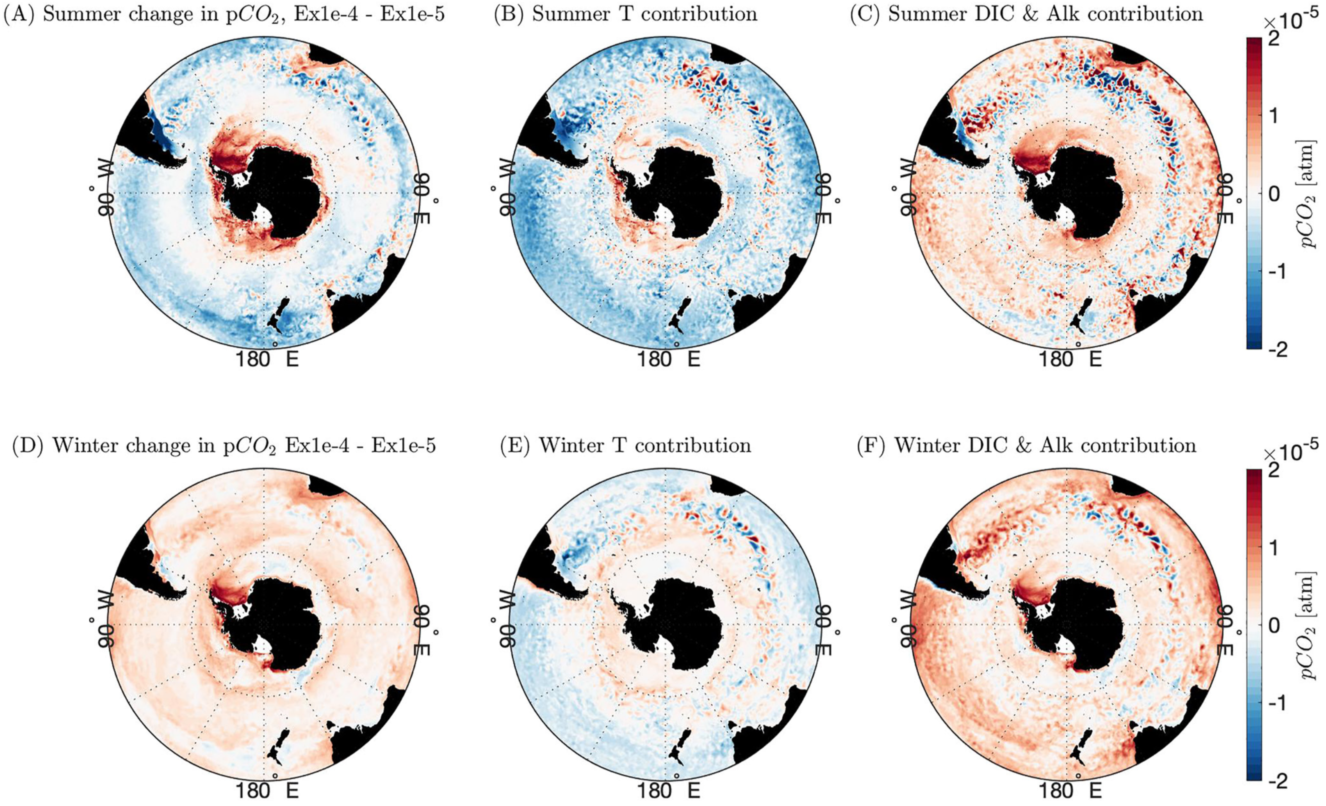

Figure 7. (a) January (summer) 2013–2018 mean change in pCO_2 (Ex1e-4–Ex1e-5) approximated by the method of Takahashi et al. (2014). (b) The contribution due to changes in temperature. (c) The contribution due to changes in carbon chemistry (DIC and Alkalinity). (d–f) Same as (a–c) but for July (winter) mean.

and its contribution to change in pCO_2 appear much smaller (Figure 4d). They are nevertheless key to driving the seasonal response of changing SO carbon fluxes in response to altered diapycnal mixing.

The vertical structure of the thermocline and the associated change in surface temperature with enhanced mixing have seasonal trends (Figures 8b and 8f). In January, surface waters are warm, and the temperature declines rapidly with depth down to 100 m, especially north of 60°S (Figure 8a). South of 60°S and below 100 m, water temperature increases with depth due to the upwelling of deep warm waters of North-Atlantic origin through Ekman transport. In Ex1e-4, subsurface cooler waters are mixed more strongly toward the surface, cooling the surface waters and warming the subsurface waters relative to Ex1e-5 (Figure 8b). This surface cooling reduces the pCO_2 (Figure 7a). In July the surface waters are well mixed and there is no temperature gradient in the upper 100 m (Figure 8e). Below the winter mixed layer, temperature rises with depth south of 60°S, and decrease with depth north of 60°S. Enhanced mixing warms surface waters, increasing the pCO_2 (Figures 7e and 7f). This increase in surface temperature also increases the rate of sea ice melt, reducing the sea ice cover toward the end of winter/spring in Ex1e-4 (Figure S3 in Supporting Information S1). This results in small regions of increased carbon uptake around the sea ice edge in winter (Figure 6f). North of 60°S and below the mixed layer, waters still decrease in temperature with depth (Figures 8e and 8f). Increased mixing cools the surface waters north of 45°S, while between 60°S and 45°S the changes in water temperature appear to be patchy. This is due to the interconnection of vertical mixing and horizontal advection by the meandering currents and eddies that lead to northward intrusion of warmer waters coming from south of 60°S. The vertical gradients of DIC and alkalinity are relatively constant regardless of season (Figures 8c and 8g). Changes in DIC and alkalinity concentrations have opposing effects on pCO_2 (Figures 4e and 4f), but together act to increase pCO_2 at all latitudes in summer and winter in Ex1e-4 (Figures 7c and 7f). The increase to pCO_2 in Ex1e-4 from combined carbonate chemistry changes is stronger in the winter than in summer, especially north of 40°S (Figures 7c and 7f).

Though all 6 years of the model run exhibit a similar seasonal cycle of changes to carbon fluxes with enhanced mixing in Ex1e-4, important interannual differences exist (Figure 9). Some differences in carbon fluxes between

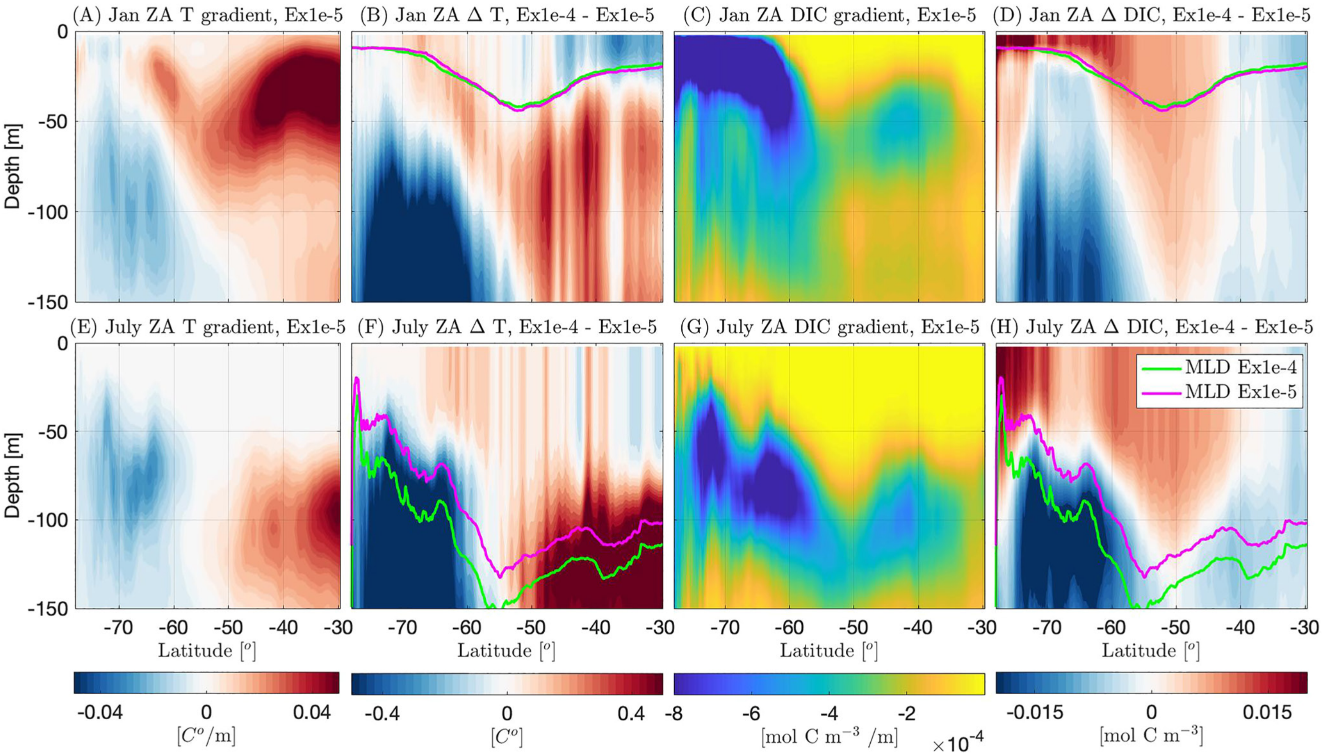

Figure 8. (a) January (2013–2018) zonally averaged (ZA) temperature vertical gradient (red implies an increase in temperature toward the surface). (b) January change in temperature (Ex1e-4–Ex1e-5). Mixed layer depth (MLD) for Ex1e-5 (pink) and Ex1e-4 (green) overlain. (c) January zonally averaged dissolved inorganic carbon (DIC) vertical gradient. (d) Change in DIC concentration (Ex1e-4–Ex1e-5). (e–h) As in (a–d) but for July (2013–2018) mean.

the two experiments become more pronounced over time, while other changes lessen. North of 40°S, Ex1e-4 has an increase in carbon uptake (or reduced outgassing) during the summer. This becomes more pronounced and extends further south down to 50°S in subsequent summers as the model run progresses. While the winter time reductions in uptake in Ex1e-4 compared to Ex1e-5 around 45°S become stronger through the 6 years, the reductions in carbon uptake south of 60°S become weaker. The SO yearly mean change in C flux (black stars, Figure 9b) between Ex1e-4 and Ex1e-5 is the greatest in the first 2 years and decreases over the subsequent 4 years. The reduced carbon fluxes in Ex1e-4 summer are primarily responsible for the smaller annual mean change observed between Ex1e-4 and Ex1e-5 in later years.

40°S approximately corresponds to the mean latitude of the subtropical front (STF) and marks a regime in terms of the leading mechanisms responsible for changes in $p\mathrm{CO_2}$ and carbon fluxes. This marks the boundary between the nutrient deplete subtropical waters to the north and the nutrient and DIC rich waters to the south (Chapman et al., 2020). Regions to the north of this divide are responsible for the summer increases in carbon uptake in Ex1e-4 in later years of the run. In contrast, regions to the south are responsible for the strong response of reduced carbon uptake in Ex1e-4.

The contributions to the total change in $p\mathrm{CO_2}$ are drastically different across the STF (Figures 9c–9e). To its south, opposite changes in $p\mathrm{CO_2}$ due to alkalinity and DIC nearly balance, with the latter being slightly larger (Figure 9d). As before, salinity contributions remain negligible at all times. Over the first 2 years of the perturbation, the total change in $p\mathrm{CO_2}$ is positive, meaning $p\mathrm{CO_2}$ is higher in Ex1e-4 than in Ex1e-5. The magnitude of the reduction in $p\mathrm{CO_2}$ due to Alkalinity increases over time. The magnitude of total $p\mathrm{CO_2}$ change decreases over time and becomes negative in the summer months, allowing for increased carbon uptake.

North of the STF, DIC and alkalinity do not balance each other out (Figure 9e) and changes in temperature between the two model runs are more dominant. Alkalinity increases $p\mathrm{CO_2}$ north of the STF, while changes in DIC initially also increase the $p\mathrm{CO_2}$ in Ex1e-4. By the summer of the third year of the run, changes in DIC begin to reduce the $p\mathrm{CO_2}$, causing the net total change in $p\mathrm{CO_2}$ to be negative in summer. This causes an increase in carbon uptake in the summer north of the STF in Ex1e-4.

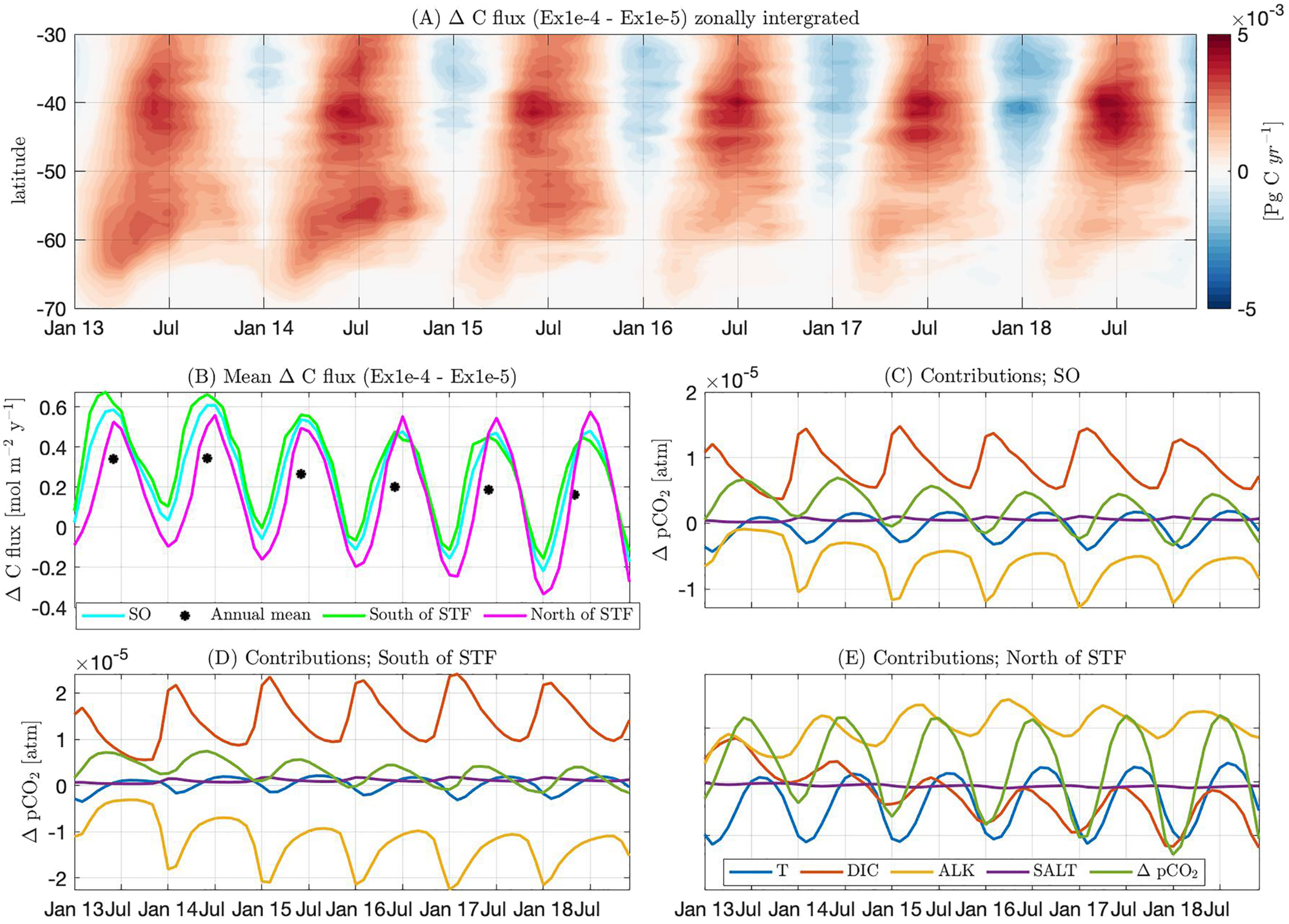

Figure 9. (a) Change in zonally integrated Carbon flux between Ex1e-4 and Ex1e-5 over the 6-year time period of January 2013 to December 2018 (Red shows reduced uptake or increased outgassing in Ex1e-4). (b) Change in the mean carbon flux across the whole Southern Ocean (SO) (blue), the SO North of the subtropical front (STF) (pink) and South of the STF (green) for the same time period. The annual mean change for the whole SO for each year is shown (black star). Using the methodology of Takahashi et al. (2014) as discussed previously, the differences in Carbon flux between the two model runs over time can be attributed to changes in surface ocean $p\mathrm{CO}_2$ (green lines) from alterations to temperature (blue lines), DIC (red lines), alkalinity (yellow lines) and salinity (purple lines). These contributions are shown for the whole SO (c), the SO south of the STF (d), and the SO north of the STF (e). The STF is defined according to the frontal definitions of Gray et al. (2018).

Almost all changes in DIC between Ex1e-4 and Ex1e-5 are due to altered diapycnal fluxes of DIC. However, north of the STF, DIC contribution to decreased $p\mathrm{CO}_2$ in the summer is due to increased productivity in the nutrient depleted waters of the subtropical gyre. This increase in productivity does not occur instantaneously, but instead takes around 6 months to begin decreasing the DIC contribution (red line, Figures 9e and 10c). While an increase in productivity occurs with higher mixing across the whole SO region, it is only in the north, roughly north of the subtropical front where increased phytoplankton production and DIC uptake becomes the dominant mechanism in altering DIC concentrations. Thus, in the context of this paper, we consider the STF as the upper boundary of the SO and postpone further discussion on the biologically dominated change in $p\mathrm{CO}_2$ north of the SO to future work.

4. Discussion

The relevance of diapycnal mixing in setting global carbon fluxes has previously been considered to be through changes to the underlying stratification and of regional and global overturning circulation and ventilation patterns. Although that may be true on centennial or longer timescales, here we show that on much faster timescales mixing directly acts upon tracers such as DIC, alkalinity, temperature, and salinity leading to a significant change in surface ocean carbon fluxes in B-SOSE. We have demonstrated that there is a strong sensitivity of carbon fluxes

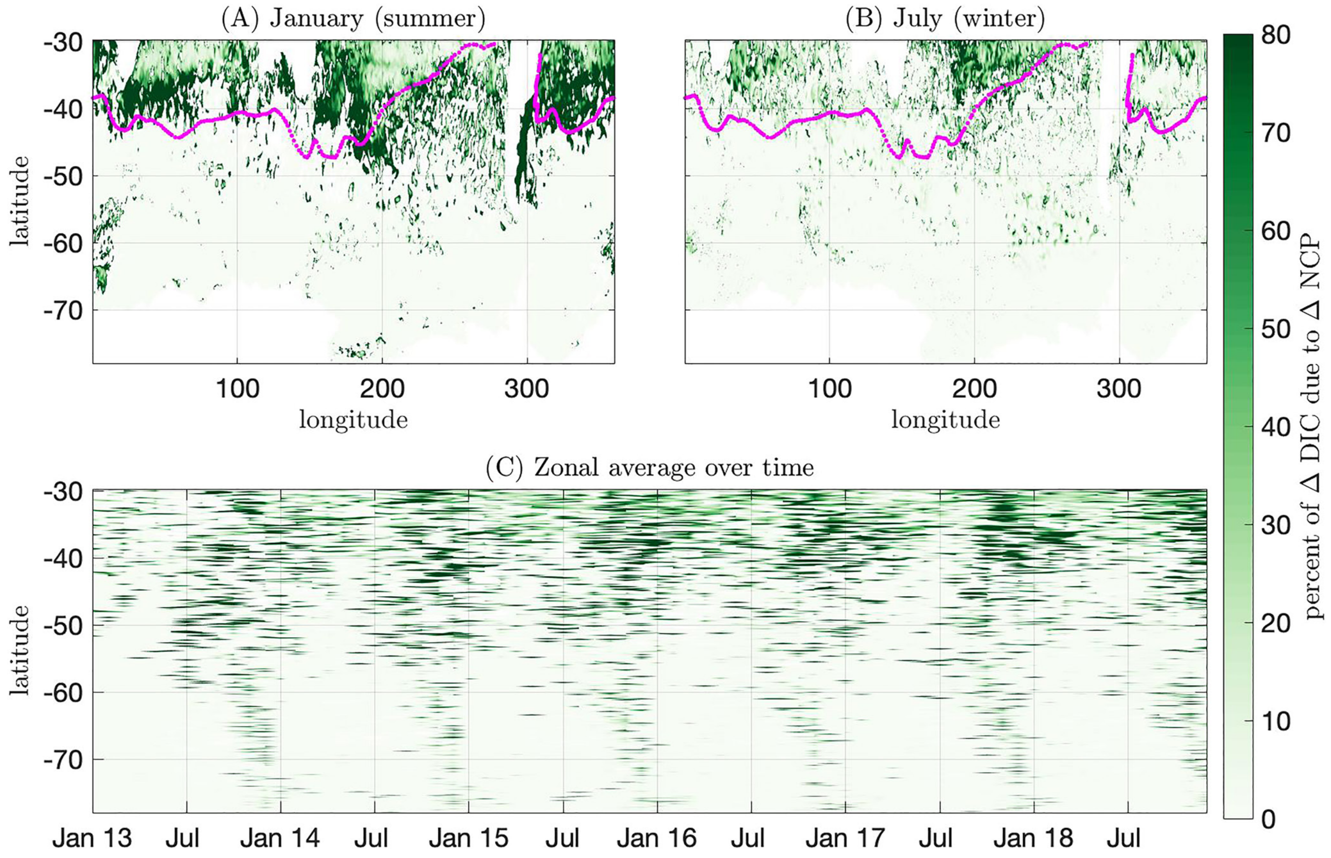

Figure 10. The percentage change of surface water dissolved inorganic carbon (DIC) concentration due to changes in biological net community productivity (NCP). Surface water is defined here as waters down to a depth of 55 m. Shown as a vertically integrated mean for (a) January (summer) and (b) July (winter). The mean location of the subtropical front, as defined by Orsi et al. (1995), is also shown in pink. (c) The zonal mean of the vertically integrated percentage change due to altered NCP is shown over time.

to immediate (less than 1 year) nonequilibrated changes in background mixing values. This mixing is known to vary by over two orders of magnitude (from 10^{-5} to 10^{-3} m^2 s^{-1}) on equally short timescales in the real ocean. A caveat is that though B-SOSE inputs are optimized to bring it into consistency with observations, biases do still exist with regard to the true ocean state (Mazloff et al., 2023). For example, Swierczek et al. (2021) showed a weaker upper ocean DIC gradient in B-SOSE than in the GLODAPv2 and BGC-Argo observations in the Argentine basin. These may impact the details of the perturbation response presented here. However, the relatively rapid and large-scale change in carbon flux in response to changing mixing is likely to be a robust signal. The results obtained may be sensitive to the initial conditions used, but we believe that the sensitivity of the system to changes in background mixing rates would occur regardless of the choice of initial conditions. Numerical mixing from horizontal diffusion operators and advection schemes acting across large isopycnal slopes are potentially more impactful to vertical exchange in the model than the explicit vertical diffusion (Ilıcak et al., 2012). For this reason, one may hypothesize that changing background mixing from 10^{-5} m^2 s^{-1} to 10^{-4} m^2 s^{-1} would have a negligible impact in B-SOSE. Nevertheless, the impact of this change is significant, suggesting this spurious diapycnal mixing must have an effective value of less than 10^{-5} m^2 s^{-1} over large regions of the model domain. While a sustained step change from 10^{-4} to 10^{-5} m^2 s^{-1} across the whole of the SO at any given time is unrealistic, variability of this order magnitude seems highly likely. Modeling temporally variable changes on small timescales which may be more representative of the background mixing rates in the SO requires more computing capacity, making it beyond the reach of this paper.

The high correlation found between vertical gradients and strong changes in tracer distributions with altered mixing shows that on a timescale of days to months, direct changes in diapycnal mixing fluxes are an important driver of $p\text{CO}_2$ variability. On longer timescales, from months to years, further feedbacks involving changes to biological productivity and mixed layer depth will also begin to cause further changes to the surface ocean $p\text{CO}_2$.

A latitudinal divide exists at around 40°S, roughly the location of the STF. High vertical tracer gradients cause the direct impact of altered tracer fluxes to dominate trends to the south, while changes in biological productivity play a key role in the observed changes to carbon fluxes to the north.

Two major issues stand in the way of better constraining of the data-assimilating ocean estimates insofar as the role of vertical mixing in the upper ocean is concerned. First, despite the significant investments in observations such as SOCAT and SOCCOM, Figure 3a clearly shows the sparsity of the available observational data. This sparseness of surface ocean $p\mathrm{CO}_2$ data and wind speeds, essential for estimating air-sea carbon fluxes due to the nonlinear interaction between gas exchange and wind speed, contributes to difficulties in modeling air-sea carbon fluxes (Bushinsky et al., 2019). From a statistical perspective, this coverage is insufficient to discern which background mixing value better represents the real ocean despite the strong impact of these choices on $p\mathrm{CO}_2$. This issue can be resolved only through sustained observations. Furthermore, the strong seasonality of the sensitivity of carbon fluxes to altered mixing demonstrates the importance of year-round observations. Despite this, the year-round SO biogeochemical observations obtained through the SOCCOM project since 2014 (Johnson et al., 2017) have helped to significantly improve our knowledge of the seasonal cycle of SO air-sea carbon fluxes (Gray et al., 2018; Prend et al., 2022).

Second, SO diapycnal mixing can vary by orders of magnitude over timescales ranging from hourly to seasonally, as well as varying spatially. Moreover, 30% of the surface area of the subpolar ocean has a synoptic variance that is greater or equal in magnitude to the summer mean interannual variance of $p\mathrm{CO}_2$, thus synoptic variability of $p\mathrm{CO}_2$ is potentially a widespread dominant mode of variability in the SO (Nicholson et al., 2022). Hence, even small variations in the synoptic entrainment flux of DIC have a large impact on the mixed layer DIC budget relative to FCO_2. To achieve a close agreement with observations, a model should have a representation of such variability. ExVar employed our best estimate of a time-mean spatially variable mixing map, resulting in carbon fluxes similar to that obtained with a constant diffusivity of 10^{-5} m^2 s^{-1}, suggesting the importance of representing temporal variability.

Finally, direct observations of diapycnal mixing in the SO have suggested that current maps such as that used in ExVar (a) lack the representation of many key processes that result in higher turbulence in upper surface waters (e.g., bottom-generated lee waves, shoaling of remotely generated internal tides) and (b) do not allow for co-variance of mixing and tracer gradients, key to biological processes. The spatial patterns of where deep waters enriched in natural carbon but lacking in anthropogenic carbon reach the upper ocean are highly localized, and are likely to be set by interior SO diapycnal transformations or by interactions with topographic mixing hot spots which cause localized upwelling (Tamsitt et al., 2017). Further work is needed to understand the distribution of upwelling sites into the surface ocean before we can begin to understand what extent these upwelling patterns influence spatial distributions of carbon fluxes (Tamsitt et al., 2017).

5. Conclusion

We have demonstrated that the air-sea carbon fluxes in the SO are highly sensitive to instantaneous changes in background mixing values well within the range of current best estimates. This is despite background mixing rates being orders of magnitude smaller than mixed layer model-generated mixing. We find that the overall changes to carbon fluxes depend on the interactive effects of changes to DIC, temperature, and alkalinity, which can compensate or reinforce each other, and the predominant driver varies regionally, seasonally and temporally as additive and opposing feedbacks kick in at varying timescales. This work highlights the absolute necessity for climate models to resolve the spatiotemporal variability of small-scale turbulent mixing, or to skillfully parameterize the processes responsible for generating them.

Data Availability Statement

The B-SOSE data sets generated during and/or analyzed during the current study are available from http://sose.ucsd.edu/SO6/ITER133_kappa_bgrd1e4/, http://sose.ucsd.edu/SO6/ITER133_kappa_bgrd1e5/ and http://sose.ucsd.edu/SO6/ITER133_tides_casimir_leew_g0p2/. The spatially variable ExVar mixing map is published via Zenodo at https://zenodo.org/record/8232709 (Ellison, Mashayek, & Mazloff, 2023).

Acknowledgments

AM acknowledges NERC Grant NE/P018319/1 and ONR Grant N00014-22-1-2082. MM acknowledges support from NSF awards OCE-1924388, OPP-1936222, and OPP-2149501, and from NASA award 80NSSC22K0387 and 80NSSC20K1076. EE was supported by the Centre for Doctoral Training Programme in sustainable environmental engineering, UK EPSRC funded. This paper benefited from feedback from two anonymous reviewers.

References

Adkins, J. F. (2013). The role of deep ocean circulation in setting glacial climates. *Paleoceanography*, *28*(3), 539–561. https://doi.org/10.1002/palo.20046

Alford, M. H. (2020). Global calculations of local and remote near-inertial-wave dissipation. *Journal of Physical Oceanography*, *50*(11), 3157–3164. https://doi.org/10.1175/JPO-D-20-0106.1

Arias, P., Bellouin, N., Coppola, E., Jones, R., Krinner, G., Marotzke, J., et al. (2021). Climate change 2021: The physical science basis. In *Contribution of working group1 I to the sixth assessment report of the intergovernmental panel on climate change*. The Intergovernmental Panel on Climate Change.

Baker, L., & Mashayek, A. (2021). Surface reflection of bottom generated oceanic lee waves. *Journal of Fluid Mechanics*, *924*, A17. https://doi.org/10.1017/jfm.2021.627

Baker, L., & Mashayek, A. (2022). The impact of representation of realistic topography on parameterized of oceanic Lee wave energy flux. *Journal of Geophysical Research: Oceans*, *127*, e2022JC018995. https://doi.org/10.1029/2022JC018995

Bakker, D. C., Pfeil, B., Landa, C. S., Metzl, N., O'Brien, K. M., Olsen, A., et al. (2016). A multi-decade record of high-quality fCO_2 data in version 3 of the Surface Ocean CO_2 Atlas (SOCAT). *Earth System Science Data*, *8*(2), 383–413. https://doi.org/10.5194/essd-8-383-2016

Bianchi, D., Galbraith, E. D., Carozza, D. A., Mislan, K., & Stock, C. A. (2013). Intensification of open-ocean oxygen depletion by vertically migrating animals. *Nature Geoscience*, *6*(7), 545–548. https://doi.org/10.1038/ngeo1837

Bushinsky, S. M., Landschützer, P., Rödenbeck, C., Gray, A. R., Baker, D., Mazloff, M. R., et al. (2019). Reassessing Southern Ocean Air-Sea CO_2 flux estimates with the addition of biogeochemical float observations. *Global Biogeochemical Cycles*, *33*, 1370–1388. https://doi.org/10.1029/2019GB006176

Cael, B., & Mashayek, A. (2021). Log-skew-normality of ocean turbulence. *Physical Review Letters*, *126*(22), 224502. https://doi.org/10.1103/physrevlett.126.224502

Chapman, C. C., Lea, M. A., Meyer, A., Sallée, J. B., & Hindell, M. (2020). Defining Southern Ocean fronts and their influence on biological and physical processes in a changing climate. *Nature Climate Change*, *10*(3), 209–219. https://doi.org/10.1038/s41558-020-0705-4

de Lavergne, C., Vic, C., Madec, G., Roquet, F., Waterhouse, A. F., Whalen, C. B., et al. (2020). A parameterization of local and remote tidal mixing. *Journal of Advances in Modeling Earth Systems*, *12*, e2020MS002065. https://doi.org/10.1029/2020MS002065

Dee, D. P., Uppala, S. M., Simmons, A. J., Berrisford, P., Poli, P., Kobayashi, S., et al., (2011). The era-interim reanalysis: Configuration and performance of the data assimilation system. *Quarterly Journal of the Royal Meteorological Society*, *137*(656), 553–597. https://doi.org/10.1002/qj.828

DeVries, T., & Primeau, F. (2011). Dynamically and observationally constrained estimates of water-mass distributions and ages in the global ocean. *Journal of Physical Oceanography*, *41*(12), 2381–2401. https://doi.org/10.1175/JPO-D-10-05011.1

Dunne, J. P., Armstrong, R. A., Gnanadesikan, A., & Sarmiento, J. L. (2005). Empirical and mechanistic models for the particle export ratio. *Global Biogeochemical Cycles*, *19*, GB4026. https://doi.org/10.1029/2004GB002390

Dutkiewicz, S., Follows, M. J., Heimbach, P., & Marshall, J. (2006). Controls on ocean productivity and air-sea carbon flux: An adjoint model sensitivity study. *Geophysical Research Letters*, *33*, L02603. https://doi.org/10.1029/2005GL024987

Dutreuil, S., Bopp, L., & Tagliabue, A. (2009). Impact of enhanced vertical mixing on marine biogeochemistry: Lessons for geo-engineering and natural variability. *Biogeosciences*, *6*(5), 901–912. https://doi.org/10.5194/bg-6-901-2009

Ellison, E., Cimoli, L., & Mashayek, A. (2023). Multi-time scale control of Southern Ocean diapycnal mixing over Atlantic tracer budgets. *Climate Dynamics*, *60*(9–10), 3039–3050. https://doi.org/10.1007/s00382-022-06428-5

Ellison, E., Mashayek, A., & Mazloff, M. (2023). The sensitivity of Southern Ocean air-sea carbon fluxes to background turbulent diapycnal mixing variability[Dataset]. Zenodo. https://doi.org/10.5281/ZENODO.8232709

Fenty, I., & Heimbach, P. (2013). Coupled sea ice-ocean-state estimation in the Labrador Sea and Baffin Bay. *Journal of Physical Oceanography*, *43*(5), 884–904. https://doi.org/10.1175/JPO-D-12-065.1

Follows, M. J., Ito, T., & Dutkiewicz, S. (2006). On the solution of the carbonate chemistry system in ocean biogeochemistry models. *Ocean Modelling*, *12*(3–4), 290–301. https://doi.org/10.1016/J.OCEMOD.2005.05.004

Galbraith, E. D., Dunne, J. P., Gnanadesikan, A., Slater, R. D., Sarmiento, J. L., Dufour, C. O., et al. (2015). Complex functionality with minimal computation: Promise and pitfalls of reduced-tracer ocean biogeochemistry models. *Journal of Advances in Modeling Earth Systems*, *7*, 2012–2028. https://doi.org/10.1002/2015MS000463

Galbraith, E. D., Gnanadesikan, A., Dunne, J. P., & Hiscock, M. R. (2010). Regional impacts of iron-light colimitation in a global biogeochemical model. *Biogeosciences*, *7*(3), 1043–1064. https://doi.org/10.5194/bg-7-1043-2010

Ganachaud, A., & Wunsch, C. (2000). Improved estimates of global ocean circulation, heat transport and mixing from hydrographic data. *Nature*, *408*(6811), 453–457. https://doi.org/10.1038/35044048

Garabato, A. C. N., Frajka-Williams, E. E., Spingys, C. P., Legg, S., Polzin, K. L., Forryan, A., et al. (2019). Rapid mixing and exchange of deep-ocean waters in an abyssal boundary current. *Proceedings of the National Academy of Sciences of the United States of America*, *116*(27), 13233–13238. https://doi.org/10.1073/pnas.1904087116

Garabato, A. C. N., Polzin, K. L., King, B. A., Heywood, K. J., & Visbeck, M. (2004). Widespread intense turbulent mixing in the Southern Ocean. *Science*, *303*(5655), 210–213. https://doi.org/10.1126/science.1090929

Garcia, H. E., Locarnini, R. A., Boyer, T. P., Antonov, J. I., Baranova, O. K., Zweng, M. M., et al. (2013). *World ocean atlas 2013. Volume 4, dissolved inorganic nutrients (phosphate, nitrate, silicate)*. National Oceanographic Data Center.

Gaspar, P., Grégoris, Y., & Lefevre, J.-M. (1990). A simple eddy kinetic energy model for simulations of the oceanic vertical mixing: Tests at station Papa and long-term upper ocean study site. *Journal of Geophysical Research*, *95*(C9), 16179–16193. https://doi.org/10.1029/JC095iC09p16179

Gray, A. R., Johnson, K. S., Bushinsky, S. M., Riser, S. C., Russell, J. L., Talley, L. D., et al. (2018). Autonomous biogeochemical floats detect significant carbon dioxide outgassing in the high-latitude Southern Ocean. *Geophysical Research Letters*, *45*, 9049–9057. https://doi.org/10.1029/2018GL078013

Gruber, N., Landschützer, P., & Lovenduski, N. S. (2019). The variable Southern Ocean carbon sink. *Annual Review of Marine Science*, *11*(1), 159–186. https://doi.org/10.1146/annurev-marine-121916-063407

Ilıcak, M., Adcroft, A. J., Griffies, S. M., & Hallberg, R. W. (2012). Spurious dianeutral mixing and the role of momentum closure. *Ocean Modelling*, *45*, 37–58. https://doi.org/10.1016/j.ocemod.2011.10.003

Johnson, K. S., Plant, J. N., Coletti, L. J., Jannasch, H. W., Sakamoto, C. M., Riser, S. C., et al. (2017). Biogeochemical sensor performance in the soccom profiling float array. *Journal of Geophysical Research: Oceans*, *122*, 6416–6436. https://doi.org/10.1002/2017JC012838

Klocker, A. (2018). Opening the window to the Southern Ocean: The role of jet dynamics. *Science Advances*, *4*(10), eaao4719. https://doi.org/10.1126/sciadv.aao4719

Landschützer, P., Gruber, N., & Bakker, D. C. E. (2016). Decadal variations and trends of the global ocean carbon sink. *Global Biogeochemical Cycles*, *30*, 1396–1417. https://doi.org/10.1002/2015GB005359

Large, W., & Yeager, S. (2009). The global climatology of an interannually varying air-sea flux data set. *Climate Dynamics*, *33*(2), 341–364. https://doi.org/10.1007/s00382-008-0441-3

Large, W. G., McWilliams, J. C., & Doney, S. C. (1994). Oceanic vertical mixing: A review and a model with a nonlocal boundary layer parameterization. *Reviews of Geophysics*, *32*(4), 363–403. https://doi.org/10.1029/94RG01872

Ledwell, J. R., St. Laurent, L. C., Girton, J. B., & Toole, J. M. (2011). Diapycnal mixing in the Antarctic circumpolar current. *Journal of Physical Oceanography*, *41*(1), 241–246. https://doi.org/10.1175/2010JPO4557.1

Losch, M., Menemenlis, D., Campin, J.-M., Heimbach, P., & Hill, C. (2010). On the formulation of sea-ice models. Part 1: Effects of different solver implementations and parameterizations. *Ocean Modelling*, *33*(1–2), 129–144. https://doi.org/10.1016/j.ocemod.2009.12.008

Lumpkin, R., & Speer, K. (2007). Global ocean meridional overturning. *Journal of Physical Oceanography*, *37*(10), 2550–2562. https://doi.org/10.1175/JPO3130.1

Mahadevan, A., Tagliabue, A., Bopp, L., Lenton, A., Mémery, L., & Lévy, M. (2011). Impact of episodic vertical fluxes on sea surface $p\mathrm{CO}_2$. *Philosophical Transactions of the Royal Society A: Mathematical, Physical & Engineering Sciences*, *369*(1943), 2009–2025. https://doi.org/10.1098/rsta.2010.0340

Marinov, I., & Gnanadesikan, A. (2011). Changes in ocean circulation and carbon storage are decoupled from air-sea CO_2 fluxes. *Biogeosciences*, *8*(2), 505–513. https://doi.org/10.5194/bg-8-505-2011

Marinov, I., Gnanadesikan, A., Sarmiento, J. L., Toggweiler, J. R., Follows, M., & Mignone, B. K. (2008). Impact of oceanic circulation on biological carbon storage in the ocean and atmospheric $p\mathrm{CO}_2$. *Global Biogeochemical Cycles*, *22*, GB3007. https://doi.org/10.1029/2007GB002958

Marshall, J., & Speer, K. (2012). Closure of the meridional overturning circulation through Southern Ocean upwelling. *Nature Geoscience*, *5*(3), 171–180. https://doi.org/10.1038/ngeo1391

Mashayek, A., Ferrari, R., Merrifield, S., Ledwell, J., St Laurent, L., & Garabato, A. (2017). Topographic enhancement of vertical turbulent mixing in the Southern Ocean. *Nature Communications*, *8*(1), 14197. https://doi.org/10.1038/ncomms14197

Mashayek, A., Reynard, N., Zhai, F., Srinivasan, K., Jelley, A., Garabato, A. N., & Caulfield, C.-C. P. (2022). Deep ocean learning of small scale turbulence. *Geophysical Research Letters*, *49*, e2022GL098039. https://doi.org/10.1029/2022GL098039

Mazloff, M. R., Heimbach, P., & Wunsch, C. (2010). An eddy-permitting Southern Ocean state estimate. *Journal of Physical Oceanography*, *40*(5), 880–899. https://doi.org/10.1175/2009JPO4236.1

Mazloff, M. R., Verdy, A., Gille, S. T., Johnson, K. S., Cornuelle, B. D., & Sarmiento, J. (2023). Southern Ocean acidification revealed by biogeochemical-argo floats. *Journal of Geophysical Research: Oceans*, *128*, e2022JC019530. https://doi.org/10.1029/2022JC019530

Melet, A., Hallberg, R., Legg, S., & Nikurashin, M. (2014). Sensitivity of the Ocean State to lee wave-driven mixing. *Journal of Physical Oceanography*, *44*(3), 900–921. https://doi.org/10.1175/JPO-D-13-072.1

Melet, A., Hallberg, R., & Marshall, D. P. (2022). The role of ocean mixing in the climate system. In *Ocean mixing* (pp. 5–34). Elsevier.

Munk, W. H. (1966). Abyssal recipes. *Deep Sea Research and Oceanographic Abstracts*, *13*(4), 707–730. https://doi.org/10.1016/0011-7471(66)90602-4

Nicholson, S.-A., Whitt, D. B., Fer, I., du Plessis, M. D., Lebéhot, A. D., Swart, S., et al. (2022). Storms drive outgassing of CO_2 in the subpolar Southern Ocean. *Nature Communications*, *13*(1), 158. https://doi.org/10.1038/s41467-021-27780-W

Nikurashin, M., & Ferrari, R. (2011). Global energy conversion rate from geostrophic flows into internal lee waves in the deep ocean. *Geophysical Research Letters*, *38*, L08610. https://doi.org/10.1029/2011GL046576

Nikurashin, M., & Ferrari, R. (2013). Overturning circulation driven by breaking internal waves in the deep ocean. *Geophysical Research Letters*, *40*, 3133–3137. https://doi.org/10.1002/grl.50542

Orsi, A. H., Whitworth, T., & Nowlin, W. D. (1995). On the meridional extent and fronts of the Antarctic Circumpolar Current. *Deep Sea Research Part I: Oceanographic Research Papers*, *42*(5), 641–673. https://doi.org/10.1016/0967-0637(95)00021-W

Peters, W., Jacobson, A. R., Sweeney, C., Andrews, A. E., Conway, T. J., Masarie, K., et al. (2007). An atmospheric perspective on north american carbon dioxide exchange: Carbontracker. *Proceedings of the National Academy of Sciences of the United States of America*, *104*(48), 18925–18930. https://doi.org/10.1073/pnas.0708986104

Prend, C. J., Hunt, J. M., Mazloff, M. R., Gille, S. T., & Talley, L. D. (2022). Controls on the boundary between thermally and non-thermally driven $p\mathrm{CO}_2$ regimes in the south pacific. *Geophysical Research Letters*, *49*, e2021GL095797. https://doi.org/10.1029/2021GL095797

Rödenbeck, C., Keeling, R. F., Bakker, D. C., Metzl, N., Olsen, A., Sabine, C., & Heimann, M. (2013). Global surface-ocean $p\mathrm{CO}_2$ and sea-air CO_2 flux variability from an observation-driven ocean mixed-layer scheme. *Ocean Science*, *9*(2), 193–216. https://doi.org/10.5194/os-9-193-2013

Rosso, I., Mazloff, M. R., Verdy, A., & Talley, L. D. (2017). Space and time variability of the Southern Ocean carbon budget. *Journal of Geophysical Research: Oceans*, *122*, 7407–7432. https://doi.org/10.1002/2016JC012646

Sarmiento, J. L., Gruber, N., Brzezinski, M. A., & Dunne, J. P. (2004). High-latitude controls of thermocline nutrients and low latitude biological productivity. *Nature*, *427*(6969), 56–60. https://doi.org/10.1038/nature02127

Schmittner, A., Urban, N. M., Keller, K., & Matthews, D. (2009). Using tracer observations to reduce the uncertainty of ocean diapycnal mixing and climate-carbon cycle projections. *Global Biogeochemical Cycles*, *23*, GB4009. https://doi.org/10.1029/2008GB003421

Shakespeare, C. J. (2020). Interdependence of internal tide and lee wave generation at abyssal hills: Global calculations. *Journal of Physical Oceanography*, *50*(3), 655–677. https://doi.org/10.1175/JPO-D-19-0179.1

Sigman, D. M., Hain, M. P., & Haug, G. H. (2010). The polar ocean and glacial cycles in atmospheric CO_2 concentration. *Nature*, *466*(7302), 47–55. https://doi.org/10.1038/nature09149

Swierczek, S., Mazloff, M. R., Morzfeld, M., & Russell, J. L. (2021). The effect of resolution on vertical heat and carbon transports in a regional ocean circulation model of the argentine basin. *Journal of Geophysical Research: Oceans*, *126*, e2021JC017235. https://doi.org/10.1029/2021JC017235

Takahashi, T., Sutherland, S. C., Chipman, D. W., Goddard, J. G., Ho, C., Newberger, T., et al. (2014). Climatological distributions of pH, $p\mathrm{CO}_2$, total CO_2, alkalinity, and CaCO_3 saturation in the global surface ocean, and temporal changes at selected locations. *Marine Chemistry*, *164*, 95–125. https://doi.org/10.1016/j.marchem.2014.06.004

Talley, L. D. (2013). Closure of the global overturning circulation through the Indian, Pacific, and Southern Oceans. *Oceanography*, *26*(1), 80–97. https://doi.org/10.5670/oceanog.2013.07

Talley, L. D., Feely, R. A., Sloyan, B. M., Wanninkhof, R., Baringer, M. O., Bullister, J. L., et al. (2016). Changes in ocean heat, carbon content, and ventilation: A review of the first decade of GO-SHIP global repeat hydrography. *Annual Review of Marine Science*, *8*(1), 185–215. https://doi.org/10.1146/annurev-marine-052915-100829

Talley, L. D., Reid, J. L., & Robbins, P. E. (2003). Data-based meridional overturning streamfunctions for the global ocean. *Journal of Climate*, *16*(19), 3213–3226. https://doi.org/10.1175/1520-0442(2003)016<3213:DMOSFT>2.0.CO;2

Tamsitt, V., Abernathey, R. P., Mazloff, M. R., Wang, J., & Talley, L. D. (2018). Transformation of deep water masses along Lagrangian upwelling pathways in the Southern Ocean. *Journal of Geophysical Research: Oceans*, *123*, 1994–2017. https://doi.org/10.1002/2017JC013409

Tamsitt, V., Drake, H. F., Morrison, A. K., Talley, L. D., Dufour, C. O., Gray, A. R., et al. (2017). Spiraling pathways of global deep waters to the surface of the Southern Ocean. *Nature Communications*, *8*(1), 172. https://doi.org/10.1038/s41467-017-00197-0

Verdy, A., & Mazloff, M. R. (2017). A data assimilating model for estimating Southern Ocean biogeochemistry. *Journal of Geophysical Research: Oceans*, *122*, 6968–6988. https://doi.org/10.1002/2016JC012650

Wanninkhof, R. (1992). Relationship between wind speed and gas exchange over the ocean. *Journal of Geophysical Research*, *97*(C5), 7373–7382. https://doi.org/10.1029/92JC00188

Waterhouse, A. F., Mackinnon, J. A., Nash, J. D., Alford, M. H., Kunze, E., Simmons, H. L., et al. (2014). Global patterns of diapycnal mixing from measurements of the turbulent dissipation rate. *Journal of Physical Oceanography*, *44*(7), 1854–1872. https://doi.org/10.1175/JPO-D-13-0104.1

Watson, A. J., Ledwell, J. R., Messias, M. J., King, B. A., Mackay, N., Meredith, M. P., et al. (2013). Rapid cross-density ocean mixing at mid-depths in the Drake Passage measured by tracer release. *Nature*, *501*(7467), 408–411. https://doi.org/10.1038/nature12432

Watson, A. J., & Naveira Garabato, A. C. (2006). The role of Southern Ocean mixing and upwelling in glacial-interglacial atmospheric CO_2 change. *Tellus Series B Chemical and Physical Meteorology*, *58*(1), 73–87. https://doi.org/10.1111/j.1600-0889.2005.00167.x